

# Twist-angle dependent proximity induced spin-orbit coupling in graphene/topological insulator heterostructures

Thomas Naimer<sup>\*</sup> and Jaroslav Fabian<sup>†</sup>

*Institute for Theoretical Physics, University of Regensburg, 93040 Regensburg, Germany*



(Received 8 February 2023; revised 1 May 2023; accepted 3 May 2023; published 23 May 2023)

The proximity-induced spin-orbit coupling (SOC) in heterostructures of twisted graphene and topological insulators (TIs)  $\text{Bi}_2\text{Se}_3$  and  $\text{Bi}_2\text{Te}_3$  is investigated from first principles. To build commensurate supercells, we strain graphene and correct thus resulting band offsets by applying a transverse electric field. We then fit the low energy electronic spectrum to an effective Hamiltonian that comprises orbital and spin-orbit terms. For twist angles  $0^\circ \leq \Theta \lesssim 20^\circ$ , we find the dominant spin-orbit couplings to be of the valley-Zeeman and Rashba types, both a few meV strong. We also observe a sign change in the induced valley-Zeeman SOC at  $\Theta \approx 10^\circ$ . Additionally, the in-plane spin structure resulting from the Rashba SOC acquires a nonzero radial component, except at  $0^\circ$  or  $30^\circ$ . At  $30^\circ$  the graphene Dirac cone interacts directly with the TI surface state. We therefore explore this twist angle in more detail, studying the effects of gating, TI thicknesses, and lateral shifts on the SOC parameters. We find, in agreement with previous results, the emergence of the proximitized Kane-Mele SOC, with a change in sign possible by electrically tuning the Dirac cone within the TI bulk band gap.

DOI: [10.1103/PhysRevB.107.195144](https://doi.org/10.1103/PhysRevB.107.195144)

## I. INTRODUCTION

Its long spin-relaxation times [1,2] and high electronic mobility [3,4] make graphene an excellent material for spin transport. However, to enable the manipulation of the spins in graphene and therefore truly unlock its full potential as a platform for spintronics, enhancing and controlling graphene's spin-orbit coupling (SOC) is necessary. Additionally, this control can enable the creation of multiple topological states [5–10]. Different features can be achieved by adding different flavors of SOC to the graphene: While Kane-Mele type SOC will lead to the formation of a quantum spin Hall effect [5,6], valley-Zeeman type SOC is needed to create spin-orbit valves [11–15] using giant spin-relaxation anisotropy [16–18]. Furthermore, Rashba type SOC will produce a Rashba Edelstein effect (charge-to-spin conversion) or even the recently discussed unconventional Rashba Edelstein effect (UREE, collinear charge-to-spin conversion) [19–23].

A very successful way of realizing such systems has been building van der Waals heterostructures [24,25], in which—due to proximity effects—electronic properties of one two-dimensional material can be transferred to another. To induce SOC in graphene, using transition-metal dichalcogenides (TMDCs, such as  $\text{WSe}_2$ ) to form graphene/TMDC heterostructures [26–30] has proven to be a viable route. Using thin layers of three-dimensional topological insulators (TIs) like  $\text{Bi}_2\text{Te}_3$  or  $\text{Bi}_2\text{Se}_3$  can introduce even larger SOC [31,32]. In experiment, such graphene/TI heterostructures can be fabricated using either exfoliation techniques [33–37] or techniques like chemical vapor deposition (CVD) [38–41]. While the former case should result in incommensurate

structures with random twist angle, the latter will produce commensurate structures with mostly fixed twist angle  $\Theta$  ( $\Theta = 0^\circ$  or  $30^\circ$ ) [38,40] between the two layers. Similar to graphene/TMDC heterostructures, the twist angle in graphene/TI heterostructures will also play a significant role for the proximity SOC that graphene obtains.

Apart from simple low energy models [42,43], a good approach for theoretically describing such heterostructures is the *ab initio* approach of density functional theory (DFT). Previous papers employing DFT for graphene/TI structures [34,37,39,44–48] focus mainly on the  $30^\circ$  supercell, while some also explore the  $0^\circ$  case [31,32]. However, intermediate twist angles have not been yet considered, although it is at those angles where symmetry allows for a radial in-plane spin structure and therefore the UREE to arise.

In this paper we make a comprehensive DFT study of the proximity SOC of graphene/ $\text{Bi}_2\text{Te}_3$  and graphene/ $\text{Bi}_2\text{Se}_3$  heterostructures for a set of commensurate supercells with different twist angles and strains. To increase the comparability between the supercells, we correct the band offsets (arising due to strain) by applying a transverse electric field, as already discussed in Ref. [49] for graphene/TMDC. We find a combination of valley-Zeeman and Rashba type SOC to be induced for all cases except  $30^\circ$ . Additionally, we observe a large twist-angle dependency of the Rashba phase angle, indicating the possibility of a purely radial in-plane spin structure ( $90^\circ$  phase angle) and UREE. A purely radial spin structure was already proposed to occur in graphene/TMDC heterostructures by a tight binding model [21]. However, DFT calculations [23,49] on such graphene/TMDC heterostructures are in disagreement with that prediction, finding a maximal phase angle of  $\pm 30^\circ$ . Furthermore, we discuss the band structure of the  $30^\circ$  supercell in more detail. Here, our results (i.e., the delicate spin structure and the unique appearance of Kane-Mele SOC)

\*thomas.naimer@physik.uni-regensburg.de

TABLE I. Lattice constants and atomic constants of unstrained primitive unit cells of graphene,  $\text{Bi}_2\text{Te}_3$  and  $\text{Bi}_2\text{Se}_3$  [51]. The structure of the TIs stays unchanged in graphene/TI supercells we use, while the graphene layers are strained by the factors  $\epsilon$  listed in Table II to ensure commensurability.

	$a$ (Å)	$c$ (Å)	$u$ (Å)	$v$ (Å)
Graphene	2.46			
$\text{Bi}_2\text{Te}_3$	4.386	30.497	$0.4000c$	$0.2097c$
$\text{Bi}_2\text{Se}_3$	4.143	28.636	$0.4008c$	$0.2117c$

are in good agreement with Ref. [31]. However, we additionally explore the effect of an external transverse electric field and find that it can change the sign of the Kane-Mele SOC.

The paper is organized as follows. In Sec. II we introduce the methodology, the supercell structures, and the procedure we apply to adjust for strain induced changes in the band offsets. Section III shows how—following Ref. [50]—the graphene Dirac cone couples to different parts of the TI first Brillouin zone (BZ) for different twist angles and strains. The model Hamiltonian used to fit the results is presented in Sec. IV. The fitting results are shown in Sec. V. We present twist angles  $0^\circ \leq \Theta \lesssim 20^\circ$  and  $\Theta = 30^\circ$  in Secs. VA and VB respectively. In Appendix A computational details are given. In Appendices B and C we discuss details of the  $30^\circ$  supercell band structure: Appendix B explains what we call “type 1” and “type 2” band pairs in the main paper and Appendix C discusses an alternative fitting Hamiltonian. In Appendices D and E the effects of varying lateral shifts and varying TI thicknesses are discussed.

## II. METHODS

The hexagonal unit cell of the TIs is described by the two lattice parameters  $a$  and  $c$  as well as the atomic constants  $u$  and  $v$  (all geometry parameters for  $\text{Bi}_2\text{Se}_3$  and  $\text{Bi}_2\text{Te}_3$  are listed in Table I). While such a unit cell contains three quintuple layers (QLs), we use, unless specified otherwise, only one QL to reduce computational effort. Due to the short range of proximity effects, the effect of additional QLs on the graphene is almost exclusively via the change of the TI surface state. Since heterostructures with  $\Theta \neq 30^\circ$  explicitly do not couple to the surface state (see Sec. III), and in accordance with the results of Ref. [32], we deem the 1QL cases to be representative for  $0 < \Theta \lesssim 20^\circ$ . We discuss 3QL cases in Appendix E and in Sec. VB, in connection with  $\Theta = 30^\circ$ . We construct the supercells by implementing the coincidence lattice method [52,53], which is detailed in Ref. [49]. We give integer attributes  $(n, m)$  to a monolayer supercell. The lattice vectors  $\mathbf{a}_{(n,m)}^S$  and  $\mathbf{b}_{(n,m)}^S$  are defined as a linear combination of the primitive lattice vectors  $\mathbf{a}$  and  $\mathbf{b}$ :

$$\mathbf{a}_{(n,m)}^S = n \cdot \mathbf{a} + m \cdot \mathbf{b}, \quad (1)$$

$$\mathbf{b}_{(n,m)}^S = -m \cdot \mathbf{a} + (n + m) \cdot \mathbf{b}. \quad (2)$$

By placing an  $(n, m)$  graphene supercell beneath an  $(n', m')$  TI supercell, we construct the graphene/TI heterostructure supercell, which then has a certain relative twist angle  $\Theta$  depending on  $n, m, n',$  and  $m'$ .

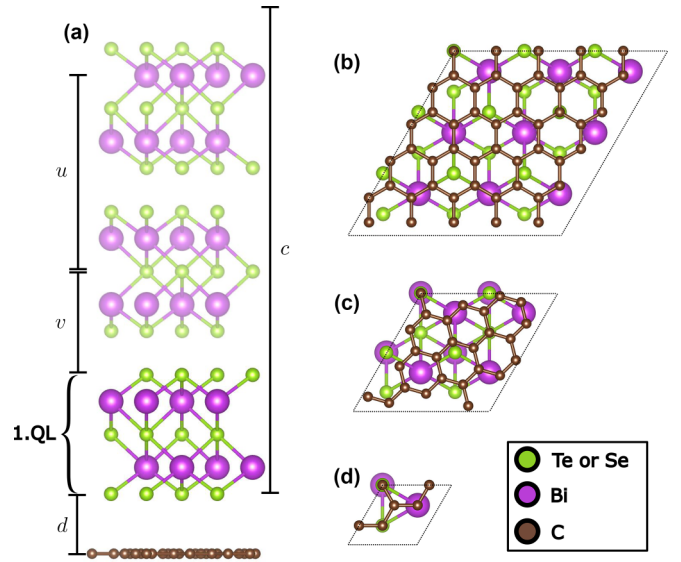


FIG. 1. (a) Side view of the  $13.9^\circ$  unit cell with indicated inter-layer distance  $d$ , atomic constants  $u$  and  $v$ , and lattice constant  $c$ . The upper two QLs are transparent, since mostly only the first QL is used in our calculations. (b–d) Bottom view of the graphene/TI heterostructure supercells with twist angles  $\Theta = 0^\circ, 13.9^\circ,$  and  $30^\circ$ , respectively.

If not specified otherwise, our supercells follow the convention of a “top” configuration. This means that at a corner of the supercell a carbon atom resides directly beneath a Te or Se atom (see Fig. 1). Considering different configurations (see Appendix D) we find that for large enough supercells the proximity SOC is rather insensitive to the changes of the atomic registry, similar to what is observed in graphene/TMDC heterostructures [27,49].

In order to obtain commensurate supercells for periodic DFT calculations, one of the layers (or both) needs to be strained. We thus introduce the strain factor  $\epsilon$ , which depends on the lattice constant of the TI and is therefore different for  $\text{Bi}_2\text{Se}_3$  and  $\text{Bi}_2\text{Te}_3$ . Since the low energy Dirac spectrum of graphene is (apart from the renormalization of the Fermi velocity) rather robust against biaxial strain smaller than 20% [54,55], we choose to leave the TI unstrained and strain graphene. Also, to focus on twist-angle effects, the used interlayer distance  $d = 3.5$  Å separating the monolayers (see Fig. 1) is the same for all studied supercells. We do not perform structural relaxation calculations for our systems assuming that—as discussed in [49] for TMDCs—this will only lead to a modification of the staggered potential (due to rippling effects) and leave the SOC parameters largely unaffected. To avoid interactions between periodic images in our slab geometry, we add a vacuum of 20 Å. All graphene/TI heterostructures are set up using the Atomic Simulation Environment [56] code. The structural parameters of the heterostructures are collected in Table II and some representative examples are visualized in Fig. 1.

In Ref. [49] we investigated graphene/TMDC heterostructures and reported a linear connection between the strain  $\epsilon$  (enforced on the graphene) and the band offset between the graphene and the TMDC band structure. For the graphene/TI

TABLE II. Structural information of the investigated graphene/TI heterostructures. Listed are the supercell attributes  $(n, m)$  of graphene and  $(n', m')$  of the TI, the resulting twist angle  $\Theta$  between the two monolayers, and the strain  $\epsilon^{\text{TI}}$  imposed on the graphene (which depends on the specific choice of TI). Additionally, we list the number of atoms ( $N_{\text{at}}$ ) in the heterostructure for the cases with one and three quintuple layers (QL) of TI. For completeness, we also list strains and  $N_{\text{at}}$  corresponding to supercells, which were not investigated, in nonboldface. These supercells, which were not investigated, either had too much built-in strain, had too many atoms, or entailed computational difficulties (e.g., convergence problems).

$\Theta$ (deg)	$(n, m)$	$(n', m')$	$\epsilon^{\text{Bi}_2\text{Te}_3}$ (%)	$\epsilon^{\text{Bi}_2\text{Se}_3}$ (%)	$N_{\text{at}}$ (1QL)	$N_{\text{at}}$ (3QL)
0.0	(0 2)	(0 1)	<b>-10.85</b>	<b>-15.79</b>	<b>13</b>	23
0.0	(0 5)	(0 3)	<b>6.98</b>	<b>1.05</b>	<b>95</b>	185
4.3	(2 3)	(1 2)	<b>8.22</b>	<b>2.22</b>	<b>73</b>	<b>143</b>
4.7	(4 3)	(2 2)	<b>1.54</b>	<b>-4.09</b>	<b>134</b>	254
8.9	(1 5)	(0 3)	<b>-3.93</b>	-9.26	<b>107</b>	197
10.9	(2 1)	(1 1)	<b>16.72</b>	<b>10.25</b>	<b>29</b>	<b>95</b>
13.9	(1 3)	(0 2)	<b>-1.1</b>	<b>-6.58</b>	<b>46</b>	<b>86</b>
16.1	(3 1)	(1 1)	<b>-14.35</b>	<b>-19.1</b>	<b>41</b>	71
17.5	(3 2)	(1 2)	<b>8.22</b>	<b>2.22</b>	<b>73</b>	143
19.1	(4 0)	(2 1)	<b>17.93</b>	<b>11.4</b>	<b>67</b>	137
19.1	(5 0)	(2 1)	<b>-5.66</b>	-10.88	<b>85</b>	155
19.1	(2 4)	(0 3)	<b>1.08</b>	<b>-4.52</b>	<b>101</b>	191
20.8	(4 3)	(1 3)	5.68	<b>-0.17</b>	<b>139</b>	269
21.1	(5 1)	(2 2)	10.93	<b>4.78</b>	<b>122</b>	242
21.8	(4 2)	(1 2)	<b>-10.85</b>	<b>-15.79</b>	<b>91</b>	161
30.0	(1 1)	(0 1)	<b>2.94</b>	<b>-2.77</b>	<b>11</b>	<b>21</b>
30.0	(7 0)	(2 2)	<b>-11.77</b>	<b>-16.66</b>	<b>158</b>	278

heterostructures we also observe a linear relation (see Fig. 2) allowing us to estimate the apparent zero-strain band offset for both cases:  $\Delta E = 396$  meV for  $\text{Bi}_2\text{Te}_3$  and  $\Delta E = 671$  meV for  $\text{Bi}_2\text{Se}_3$ . We then apply a transverse electric field to each supercell to reduce the band offset to the zero-strain one.

As a reference point for the TI energies we use the TI surface state (or for the 1QL case the remnants of the surface state) at  $\Gamma$ . Unlike thin TMDC monolayers, the TI multilayers we use are rather thick, having a thickness of  $\approx 7$  Å per QL. This makes them more vulnerable for unwanted side effects of the electric field to the band structure. A prominent example is the splitting of the TI surface state [57] into a state living at the lower TI surface (close to the graphene monolayer) and one living at the upper TI surface (further away from the graphene monolayer). However, we expect the consequences for the proximity SOC to be rather minimal, since the proximity SOC is induced mainly by the atomic orbitals close to the graphene monolayer in real space.

The computational methodology for obtaining DFT electronic band structures of the graphene/TI supercells is detailed in Appendix A.

### III. QUALITATIVE PICTURE OF INTERLAYER INTERACTION IN K SPACE

Reference [50] details by generalized Umklapp processes how in twisted heterostructures only certain  $k$  points of the two layers can interact with each other. In the graphene/TI

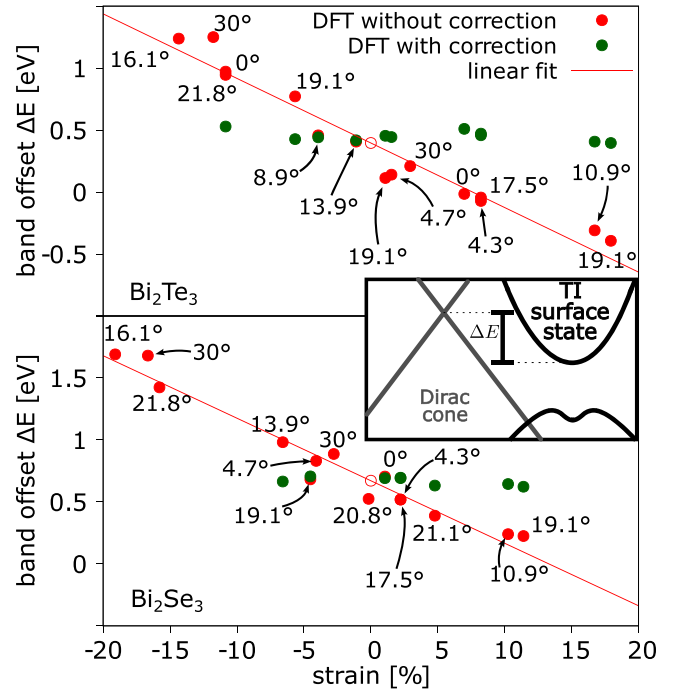


FIG. 2. Correcting for the strain induced band offset changes. For all the investigated supercells of graphene with 1QL of  $\text{Bi}_2\text{Te}_3$  and  $\text{Bi}_2\text{Se}_3$  we plot the band offsets  $\Delta E$  of the Dirac cone with respect to the remnant of the TI surface state (see inset) against the strain on graphene  $\epsilon$ ;  $\epsilon > 0$  indicates tensile strain while  $\epsilon < 0$  indicates compressive strain. Each of the data points (red solid circles) is annotated with the twist angle of the corresponding supercell. From the linear fit (red line) we extract the (apparent) zero-strain band offsets (empty red circles). The green circles show the band offsets after the correction by the transverse electric field employed to compensate the influence of strain. The inset shows schematically how the band offset  $\Delta E$  is measured.

heterostructures our focus is on the graphene low energy Dirac states. Therefore we are interested in the  $k$  points in the two-dimensional primitive TI ( $\text{Bi}_2\text{Se}_3$  or  $\text{Bi}_2\text{Te}_3$ ) unit cell, with which the Dirac cone of graphene will primarily interact (and obtain its SOC from) in a graphene/TI heterostructure. The principle contribution comes from three  $k$  points, which are equivalent due to symmetry. The location of these  $k$  points depends both on the twist angle between the two materials and the ratio of their lattice constants, so in this case  $a_{\text{TI}}/a_{\text{Gr}}$ . Since the strain we apply to the graphene in order to construct a commensurate heterostructure changes  $a_{\text{TI}}/a_{\text{Gr}}$ , we can identify strain and twist angle as the two relevant factors for our calculations. Figure 3 shows for both  $\text{Bi}_2\text{Se}_3$  and  $\text{Bi}_2\text{Te}_3$  where those  $k$  points lie for the supercells listed in Table II.

As is also clear from Fig. 3, for the  $30^\circ$  supercell the graphene Dirac cone interacts exactly with the  $\Gamma$  point of the TI. Since this is the reciprocal lattice momentum at which the surface states of the TI reside, this particular twist angle is expected to be special. Indeed, Ref. [31] reports SOC of the Kane-Mele type appearing in DFT calculations on a graphene/ $\text{Bi}_2\text{Se}_3$  heterostructure with a  $30^\circ$  twist angle. We dedicate Sec. VB to discussing this special case.

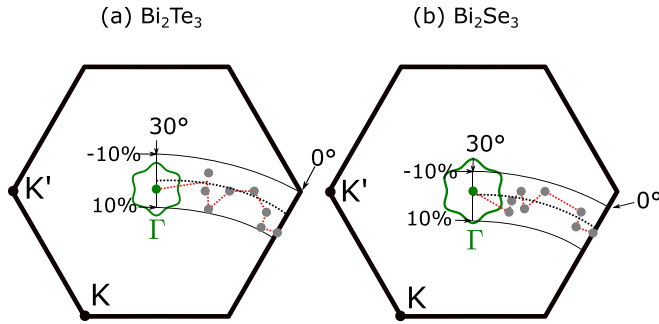


FIG. 3. Two-dimensional first BZ of (a)  $\text{Bi}_2\text{Te}_3$  and (b)  $\text{Bi}_2\text{Se}_3$ . The green dot marks the  $\Gamma$  point, with the green line indicating the cross section of the TI surface state (for the 1 QL case) at the height of the electric field corrected Dirac cone energy. For each calculated supercell the  $k$  points to which the Dirac cone couples are drawn (after symmetry reduction). Additionally, the zero-strain line is drawn (dotted line), formed by all points of hypothetical supercells with  $\epsilon = 0\%$  and  $0^\circ \leq \Theta \leq 30^\circ$ . The outlined sector indicates all relevant  $k$  points for a range of  $-10 \leq \epsilon \leq 10\%$  and  $0^\circ \leq \Theta \leq 30^\circ$ . The red line connects all DFT data points with  $\epsilon < 10\%$  and represents the sequence of points in Fig. 5.

#### IV. EFFECTIVE HAMILTONIAN

In order to find the twist-angle dependence of the proximity induced SOC in graphene's Dirac bands due to the coupling with the TIs, we fit the DFT band structures at the Dirac points to a model Hamiltonian [26]. The Hamiltonian  $H$  comprises the orbital part  $H_{\text{orb}}$  and the spin-orbit part  $H_{\text{SO}}$ . The latter is composed of the intrinsic spin-orbit coupling  $H_{\text{SO},I}$  and the Rashba coupling  $H_{\text{SO},R}$ :

$$H(k) = H_{\text{orb}}(k) + H_{\text{SO}} = H_{\text{orb}}(k) + H_{\text{SO},I} + H_{\text{SO},R}. \quad (3)$$

The orbital part describes the dispersion of the graphene Dirac cone linearized around the  $K/K'$  point; accordingly,  $k$  is the electron wave vector measured from  $K/K'$ . It also includes a staggered potential  $\Delta$ , caused by the substrate's asymmetrical influence on the graphene  $A$  and  $B$  sublattice:

$$H_{\text{orb}}(k) = \hbar v_F (\kappa \sigma_x k_x + \sigma_y k_y) + \Delta \sigma_z. \quad (4)$$

Here,  $v_F$  is the Fermi velocity of the Dirac electrons and  $\sigma$  are the Pauli matrices operating on the sublattice ( $A/B$ ) space. The parameter  $\kappa = 1$  for  $K$  and  $\kappa = -1$  for  $K'$ .

The intrinsic spin-orbit Hamiltonian

$$H_{\text{SO},I} = [\lambda_{\text{KM}} \sigma_z + \lambda_{\text{VZ}} \sigma_0] \kappa \sigma_z, \quad (5)$$

and the Rashba spin-orbit Hamiltonian

$$H_{\text{SO},R} = -\lambda_R \exp\left(-i\Phi \frac{s_z}{2}\right) [\kappa \sigma_x s_y - \sigma_y s_x] \exp\left(i\Phi \frac{s_z}{2}\right), \quad (6)$$

both additionally act on the spin space, which is described by the spin Pauli matrices  $s_x$ ,  $s_y$ , and  $s_z$ ;  $\lambda_{\text{VZ}}$  and  $\lambda_{\text{KM}}$  are the valley-Zeeman [26,29] SOC (sublattice-odd) and the Kane-Mele [5] SOC (sublattice-even) respectively. The Rashba SOC term is defined by a magnitude  $|\lambda_R|$  and a phase angle  $\Phi$ . The latter is present in  $C_3$  symmetric structures [49,58,59] and rotates the spin texture about the  $z$  axis, adding a radial component to the Rashba field.

We choose to limit the Rashba parameter to positive values  $\lambda_R > 0$ . A sign change of  $\lambda_R$  then corresponds to an additional phase shift of  $\Phi$  by a half rotation, i.e.,  $\Phi \rightarrow \Phi + 180^\circ$ . To make this clear we always write  $|\lambda_R|$ .

We only construct heterostructure with angles between  $0^\circ$  and  $30^\circ$ . The parameters for all other twist angles can be obtained by the following symmetry rules.

Twisting clockwise or counterclockwise from  $0^\circ$  influences only the Rashba phase angle:

$$\lambda_{\text{VZ}}(-\Theta) = \lambda_{\text{VZ}}(\Theta), \quad (7)$$

$$|\lambda_R(-\Theta)| = |\lambda_R(\Theta)|, \quad (8)$$

$$\Phi(-\Theta) = -\Phi(\Theta), \quad (9)$$

$$\Delta(-\Theta) = \Delta(\Theta). \quad (10)$$

Additionally a twist by  $60^\circ$  corresponds to switching the sublattices of graphene and therefore changes the sign of the sublattice-sensitive parameters:

$$\lambda_{\text{VZ}}(\Theta + 60^\circ) = -\lambda_{\text{VZ}}(\Theta), \quad (11)$$

$$|\lambda_R(\Theta + 60^\circ)| = |\lambda_R(\Theta)|, \quad (12)$$

$$\Phi(\Theta + 60^\circ) = \Phi(\Theta), \quad (13)$$

$$\Delta(\Theta + 60^\circ) = -\Delta(\Theta). \quad (14)$$

#### V. RESULTS

We calculate the electronic band structures for all supercells listed in boldface in Table II by means of DFT for the 1QL case. Figure 4 shows a few representative band structures. In addition it shows zooms to the graphene Dirac cone and the in-plane spin structure around it. It is clearly visible that the proximity SOC and therefore the structure of the Dirac cone are different for different angles. Fitting the Dirac cones to the model Hamiltonian, Eq. (3), results in effective model parameters (see Table III) which can be used to compare different twist angles. In the following, we discuss these results separately for twist angles below  $20^\circ$  and for the twist angle at  $30^\circ$ , as the two cases have distinct features.

##### A. Results I: $0^\circ \leq \Theta \lesssim 20^\circ$

For twist angles  $0^\circ \leq \Theta \lesssim 20^\circ$  the graphene Dirac point acquires its SOC mainly from parts of the TI first BZ which are away from the  $\Gamma$  point. The corresponding Bloch states are not what would form TI surface states, as those appear at  $\Gamma$ . Hence, the overall SOC is weaker than for the  $\Theta = 30^\circ$  case (see next subsection). Additionally, the SOC has similar functional form to that in graphene/TMDC heterostructures [49]: both staggered potential  $\Delta$  and  $\lambda_{\text{KM}}$  are negligibly small, while  $\lambda_{\text{VZ}}$  and  $|\lambda_R|$  dominate. This is in agreement with earlier calculations [31,57]. Also, the Rashba phase angle vanishes ( $\Phi = 180^\circ$ ) for  $\Theta = 0^\circ$  due to symmetry.

Figure 5 depicts the twist-angle dependence of the extracted SOC parameters  $\lambda_{\text{VZ}}$ ,  $|\lambda_R|$ , and  $\Phi$ . The qualitative structure is the same for both materials  $\text{Bi}_2\text{Se}_3$  and  $\text{Bi}_2\text{Te}_3$ . It exhibits a special feature of the graphene/TI heterostructures,

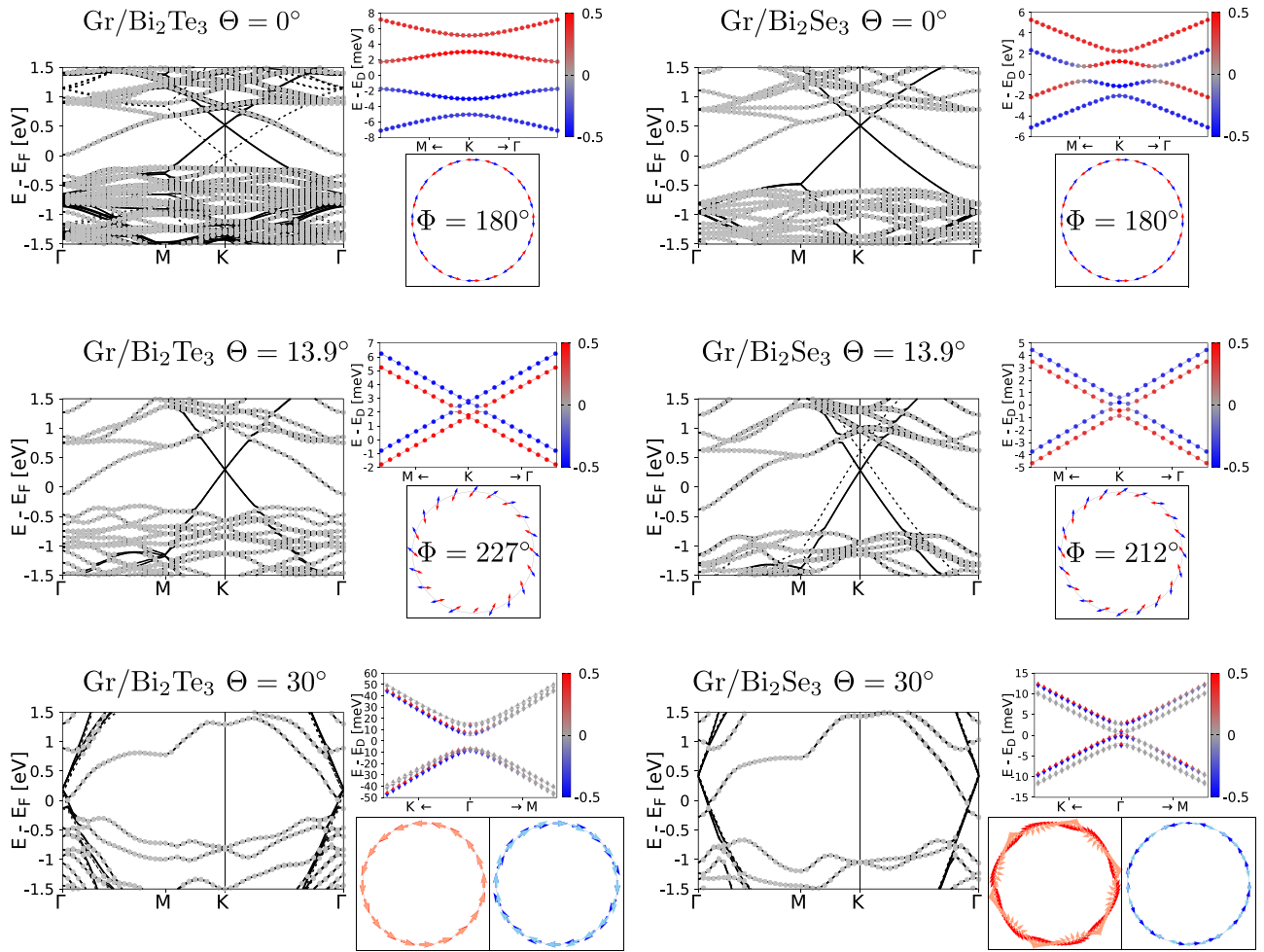


FIG. 4. Calculated band structures of graphene/TI heterostructures using  $\text{Bi}_2\text{Te}_3$  (first column),  $\text{Bi}_2\text{Se}_3$  (second column), and three different selected twisting angles  $\Theta = 0^\circ, 13.9^\circ, 30^\circ$ . The gray circles indicate states originating from TI orbitals, while the solid (dashed) lines come from graphene states with (without) the electric field corrections. For the low-strain cases ( $\text{Gr}/\text{Bi}_2\text{Te}_3$   $13.9^\circ$ ,  $\text{Gr}/\text{Bi}_2\text{Se}_3$   $0^\circ$  and both  $30^\circ$  cases) the solid and dashed lines coincide, because no strong shifting electric field is needed. The origin of the energy scale is set to zero for the Fermi energy of the band structures without electric field correction. The remnant of the TI surface state can be seen at  $\Gamma$ . Because of band folding effects, the graphene Dirac cone resides at the  $k$  point for all angles except  $\Theta = 30^\circ$ . In addition to the band structures along high symmetry lines, we show zooms to the (electric field corrected) Dirac cone with color coded spin and the in-plane spin structure along a circular path around the Dirac cone at  $\approx 55$  meV. For the zooms, dots show DFT data while solid lines represent the fits from the model Hamiltonian [Eq. (3)]. In the circular-path plots, red (blue) arrows indicate in-plane spin in the energetically lower (higher) valence band. For  $\Theta = 0^\circ$  the colors coincide with spin  $z$ , but (due to the sign change in  $\lambda_{VZ}$ ) they do not for  $\Theta = 13.9^\circ$ . Since for  $\Theta = 30^\circ$  the band structure comprises eight bands, we show two plots with red and orange (blue and light-blue) arrows indicating the energetically lower (higher) pair of valence bands. Conduction bands show the same structure. The Rashba phase angles  $\Phi$  are extracted for all but the  $\Theta = 30^\circ$  case. Note that for the zoomed band structures of the  $\Theta = 30^\circ$  cases the  $k$  window is enlarged by a factor of 3 ( $\text{Bi}_2\text{Se}_3$ ) or 15 ( $\text{Bi}_2\text{Te}_3$ ).

namely, the sign change of  $\lambda_{VZ}$  at about  $\Theta = 10^\circ$ . Since increasing the TI thickness from 1QL to 3QL leaves the sign of  $\lambda_{VZ}$  unaffected (see Appendix E), it is reasonable to conjecture, taking into account the short range of the proximity effect in van der Waals heterostructures, that the valley-Zeeman SOC changes sign also for graphene on bulk TI.

Since heterostructures with large strain ( $\epsilon < 10\%$ ) couple to very different parts of the TI Brillouin zone, they deviate strongly from the zero-strain path in Fig. 3 and are therefore depicted as transparent points in Fig. 5. Nevertheless, we can infer from these calculations that there can be a sign change not only by sweeping the twist angle  $\Theta$ , but also by sweeping the strain  $\epsilon$ . E.g., a graphene/ $\text{Bi}_2\text{Te}_3$  heterostructure with a fixed twist angle of  $19.1^\circ$  changes the sign of  $\lambda_{VZ}$ , when

going from moderate strains ( $\epsilon_1 = -5.66\%$ ,  $\epsilon_2 = 1.08\%$ ) to a very large positive strain ( $\epsilon_3 = 17.93\%$ ). We estimate this sign change to happen at 8 to 10% for twist angles  $\Theta > 10^\circ$ . Although such heterostructures are not directly realizable in an experiment (due to the large strain), it is a relevant side note for heterostructures using similar TIs or alloys of TIs, which have slightly different lattice constants. The sign changes are visualized in the second line of Fig. 5.

Remarkably, there are two irregularities that appear. First, there is a rather abrupt sign change in  $\lambda_{VZ}$  between the two last data points ( $\Theta = 20.8^\circ$  and  $21.1^\circ$ ) of the  $\text{Bi}_2\text{Se}_3$  heterostructures in Fig. 5(b). This could be due to the close vicinity of the Dirac cone of the  $\Theta = 21.1^\circ$  heterostructure to the TI surface state: Despite the rather small difference in twist

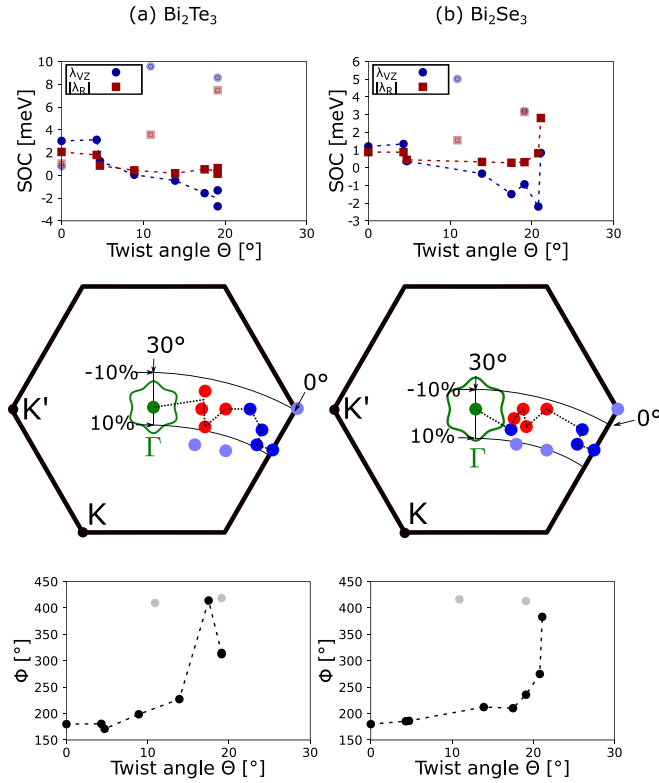


FIG. 5. Calculated SOC parameters of the graphene Dirac cone proximitized by (a)  $\text{Bi}_2\text{Te}_3$  and (b)  $\text{Bi}_2\text{Se}_3$ . The effect of strain is corrected by transverse electric field, as described in Sec. II. The first line of plots shows Rashba SOC  $|\lambda_R|$  (red squares) and valley-Zeeman SOC  $\lambda_{VZ}$  (blue circles) as a function of the twist angle  $\Theta$ . Data points from supercells with excessive built-in strain of  $\epsilon > 10\%$  are deemphasized (transparent). The dotted line is a guide for the eyes. The second line of plots shows the TI Brillouin zone and filled circles indicating regions in which the Dirac cone couples to the TI Bloch states, as in Fig. 3. Blue symbols correspond to positive valley-Zeeman SOC  $\lambda_{VZ} > 0$ , while red symbols correspond to negative valley Zeeman SOC  $\lambda_{VZ} < 0$ . The green circle represents the  $\Gamma$  point as well as the  $30^\circ$  supercell connecting to it. The dotted line connects the relevant points with ascending twist angle in the same order as the guide to the eyes in the first line of plots. The third line of plots shows the twist-angle dependence of the Rashba phase angle  $\Phi$ . Again, data points with  $\epsilon > 10\%$  are deemphasized (gray).

angle, due to its different strain its Dirac cone couples to a point closer to the  $\Gamma$ - $M$  line rather than the  $\Gamma$ - $K$  line. Since in this direction in  $k$  space the slope of the TI surface state is less steep, it is closer to the Dirac cone in energy. And apparently this influence manifests in the sign change of  $\lambda_{VZ}$ . Secondly, the magnitude  $|\lambda_R|$  of the Rashba SOC is generally smaller than the magnitude of  $\lambda_{VZ}$ . It seems to almost monotonically decrease for  $0^\circ \leq \Theta \lesssim 20^\circ$ . However, when looking again at the  $\Theta = 21.1^\circ$   $\text{Bi}_2\text{Se}_3$  data point, we see a strong increase of  $|\lambda_R|$ , again likely related to the Dirac cone's vicinity to the remnants of the surface state.

The Rashba phase angle  $\Phi$  is essential for collinear charge-to-spin conversion [19–23], since for  $\Phi = 0^\circ$  and  $180^\circ$  collinear charge-to-spin conversion is forbidden. The twist-angle dependence of  $\Phi$  in graphene-based heterostructures is

not well explored apart from the symmetry-dictated fact that  $\Theta = 0^\circ$  and  $30^\circ$  both entail  $\Phi = 0^\circ$  or  $180^\circ$  [21,49,58].

For intermediate twist angles  $0^\circ < \Theta < 30^\circ$ , there can be either no sign change  $\Phi(\Theta = 0^\circ) = \Phi(\Theta = 30^\circ)$  or a sign change  $\Phi(\Theta = 0^\circ) = \Phi(\Theta = 30^\circ) + 180^\circ$ . The latter is especially interesting, since it implies the existence of a twist angle  $0^\circ < \Theta < 30^\circ$  for which  $\Phi = 90^\circ$  or  $270^\circ$  and therefore a purely radial Rashba spin structure and purely collinear charge-to-spin conversion. Reference [21] predicts such a sign change to happen for certain graphene/TMDC heterostructures based on a tight binding model, although DFT results [23,49] are at odds with that prediction. Our results seem to strongly indicate that such a sign change could occur for graphene/TI heterostructures with the twist angle corresponding to a purely radial spin structure being  $\Theta \approx 18^\circ$  (see Fig. 5).

### B. Results II: $\Theta = 30^\circ$

By combining a  $\sqrt{3} \times \sqrt{3}$  graphene supercell ( $n = m = 1$ ) and a  $1 \times 1$  TI supercell ( $n' = 0, m' = 1$ ) one can create a heterostructure with a twist angle of  $\Theta = 30^\circ$ . Even though other heterostructures with such a twist angle can be constructed (e.g.,  $n = 7, m = 0, n' = m' = 2$ ), the former is unique in a few ways.

(1) It is a notably small supercell. For larger heterostructures the shifting degree of freedom is mostly irrelevant for the proximity SOC, because the graphene will have many different local atomic registries, which will always result in some average proximity effect. Since this is impossible for such a small supercell, the shifting degree of freedom will strongly affect the low energy Dirac cone band structure (see Appendix D).

(2) The  $K$  and  $K'$  points of the primitive graphene first Brillouin zone are folding back to the  $\Gamma$  point of the supercell's first Brillouin zone, creating an eight band Dirac cone.

(3) Not only will the Dirac cones fold back to the  $\Gamma$  point, but, more significantly, the point of the TI BZ with which the graphene Dirac cone will interact by the theory of generalized Umklapp processes (see Sec. III and Ref. [50]) is exactly the  $\Gamma$  point, where the TI surface state resides.

According to the first point, we observe very different low energy spectra for the four different shifting configurations (see Fig. 9). For all but the “hollow” configuration we see eight distinct bands, degenerate only at the  $\Gamma$  point, where Cramer's rule strictly demands it. The hollow configuration is the energetically most favorable one and therefore the one we will focus on (all plots in the main paper regarding the  $\Theta = 30^\circ$  supercell represent this hollow case). It entails band structures consisting of four band pairs with energy splittings within such a band pair being on the  $\mu\text{eV}$  range. These small splittings lead to a certain spin structure (see Appendix B), that has also been found and discussed in Ref. [31]. However, since the splitting is very small and the resulting spin structure is very elusive, we only use the simple Hamiltonian [Eq. (3)] described in Sec. IV for the fittings in the main paper (we reduce the eight bands to four by ignoring one band of each almost-degenerate band pair). This on the one hand allows for better comparability with the parameters of the other twist angles, but on the other hand fails to describe the spin structure.

In Appendix C we fit the Dirac cones with an alternative fitting Hamiltonian which is akin to the one used in Ref. [31] and find that the fitting parameters are very similar.

Due to the aforementioned backfolding, we cannot include spin- $z$  expectation values in the fitting procedure. However, pseudospin (sublattice imbalance) is used in addition to the energies to unambiguously determine the correct parameters. For the hollow case pseudospin is always zero, therefore demanding  $\Delta = \lambda_{VZ} = 0$  (this can alternatively be deduced from symmetry). For the top case the pseudospins of the eight bands form a complicated structure, which can be roughly reproduced using a full tight binding model Hamiltonian including certain onsite potentials (see Appendix D). The energies and pseudospins of the “bridge” case could not be sufficiently reproduced by either Hamiltonian.

The in-plane spin structure of the graphene/Bi<sub>2</sub>Se<sub>3</sub> 30° case (see Fig. 4, right column, last line) can clearly not be described with the Hamiltonian in Eq. (3). For the graphene/Bi<sub>2</sub>Te<sub>3</sub> 30° case (see Fig. 4, left column, last line) the band pairs seem to exhibit a typical tangential Rashba in-plane spin structure. However, the order in which clockwise (c) or counterclockwise (cc) spin structures appear (starting from the energetically lowest band pair) is alternating, i.e., cc-c-cc-c. For the usual Rashba case it is cc-c-c-cc. Therefore, the in-plane spin structures also cannot be described by Eq. (3) and we cannot estimate a Rashba phase angle from such calculations. This means there appears to be physics in the commensurate system, which the simple model Hamiltonian [Eq. (3)] is not able to capture. Assuming that this physics stems from the specific atomic registry dependence, an unstrained incommensurate structure should still be well described by the simple model Hamiltonian [Eq. (3)]. Based on the results from the last line of plots of Fig. 5, we presume that the phase angle  $\Phi$  of such an incommensurate structure will be shifted by 180° with respect to the one at  $\Theta = 0^\circ$ . Experimentally, a commensurate structure could be the result of CVD or molecular beam epitaxy fabrication, while the incommensurate structure might be obtained by an exfoliation method.

For  $0^\circ \leq \Theta \lesssim 20^\circ$  the Dirac cone lies (locally) within a band gap. As already mentioned for  $\Theta = 30^\circ$  the Dirac cone now lies directly on top of the TI surface state at the  $\Gamma$  point. Therefore, both the thickness of the TI (determining the concrete form of the surface state) and an applied transversal electric field (determining the relative position of the Dirac cone with respect to the surface state) can be expected to strongly influence the proximity SOC induced in the graphene. In the following, we will focus on the hollow shifting configuration, since it is the energetically most favorable.

In Fig. 6 we show the electric field dependence of the parameters for the 1QL case and the 3QL case. The Dirac cone is shifted through the range marked in black within the TI band structure using an electric field. With  $\Delta = \lambda_{VZ} = 0$  as stated before, the two remaining parameters  $\lambda_{KM}$  and  $|\lambda_R|$  are both in the meV range. When the Dirac cone comes close to a TI band, the SOC becomes larger with both parameters reaching up to 20 meV in magnitude. Parameter  $\lambda_{KM}$  can remarkably change sign whilst the Dirac cone moves from one band to another. Additionally, we depict the orbital

decomposition of the Dirac cone. The black curve, showing the general TI content and therefore the strength of the proximity effect, will unsurprisingly increase when nearing one of the TI bands. We find TI  $p$  orbitals to be contributing the most to the proximity effects ( $\approx 90\%$ ), while  $s$  orbitals contribute to a less, but still significant, amount ( $\approx 10\%$ ). The dark green curve shows that this distribution stays roughly constant, when shifting the Dirac cone, with a tendency for higher  $s$ -orbital content near the surface state. The  $d$ -orbital contribution is negligibly small. Distinguishing even further, we investigated the percentage of  $p$  orbitals with  $m_j = \pm 3/2$  and  $\pm 1/2$ . This distinction is essentially the equivalent of distinguishing between  $p_{x/y}$  and  $p_z$  orbitals in a spinless case, only now that SOC is present  $m_l$  is not a good quantum number and must be replaced with  $m_j$ . We find that the  $m_j = \pm 3/2$  orbitals make up roughly 20% of the contributing  $p$  orbitals, which is rather high, considering the Dirac cone  $p_z$  orbitals overlap more with other  $p_z$  orbitals and that the TI bands near the Dirac cone consist of hardly any states with  $m_j = \pm 3/2$ . We conclude that an astonishingly large contribution to the proximity effect is coming from bands more than 2 eV away from the Dirac cone in the valence and conduction band, rather than from the surface state itself. Therefore, when the Dirac cone approaches any nearby band with low  $m_j = \pm 3/2$  content, it will acquire a significant proximity effect from it and the relative contribution of the deep-lying states decreases. This corresponds to a decline of the yellow curve indicating relative  $m_j = \pm 3/2$   $p$ -orbital content.

Another interesting feature of the band structure is the separation into two distinct kinds of band pairs, occurring in an alternating fashion. One of those kinds of band pairs inherits its properties (mainly spin structure and orbital composition) from the nearby surface state, while the other one inherits its properties from the deep-lying states. This distinction is described in Appendix B in detail.

## VI. SUMMARY

We systematically investigated the proximity induced SOC in twisted graphene/Bi<sub>2</sub>Se<sub>3</sub> and graphene/Bi<sub>2</sub>Te<sub>3</sub> heterostructures. After determining an approximate zero-strain band offset, we correct the band offset of all structures accordingly and fit their energies and spin to an established SOC Hamiltonian to extract relevant SOC parameters. We separately consider supercells in a twist-angle range  $0^\circ \leq \Theta \lesssim 20^\circ$ , which are barely affected by the TI surface state, and one special highly commensurate supercell at  $\Theta = 30^\circ$ , which is heavily influenced by the surface state. For the  $0^\circ \leq \Theta \lesssim 20^\circ$  supercells we extract the twist-angle dependence of the relevant types of SOC, which are valley-Zeeman ( $\lambda_{VZ}$ ) and Rashba ( $|\lambda_R|$ ,  $\Phi$ ). Upon twisting, we witness a change of the valley-Zeeman sign at  $\Theta \approx 10^\circ$ . Additionally we witness a sign change upon changing the strain at about +8 to +10% strain for twist angles  $\Theta > 10^\circ$ . We confirm that the Rashba phase angle  $\Phi$  has a value of  $\Phi = 180^\circ$  at  $\Theta = 0^\circ$ . For increasing twist angle the phase angle  $\Phi$  also increases and crosses  $\Phi = 270^\circ$  for  $\Theta \approx 18^\circ$ , where a purely radial in-plane spin structure occurs. Assuming that this trend continues for twist angles  $\Theta > 20^\circ$ , it seems likely that (for incommensurate heterostructures) the

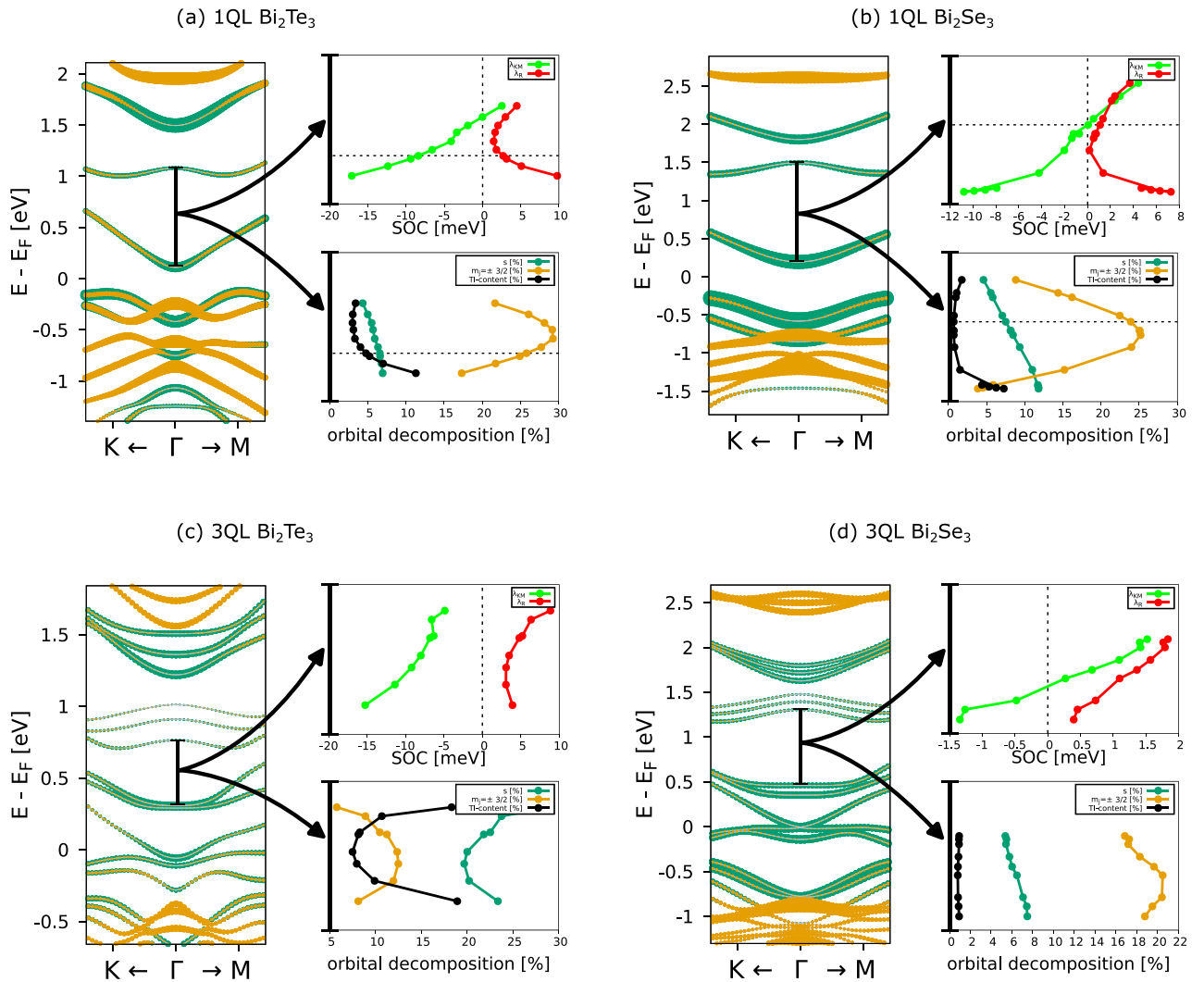


FIG. 6. Electric field dependence of fitting parameters for the  $30^\circ$  supercell: We show the band structure of 1QL or 3QL of  $\text{Bi}_2\text{Te}_3$  or  $\text{Bi}_2\text{Se}_3$  around the  $\Gamma$  point along high symmetry lines. The color code represents the projection of the state onto the TI  $s$  orbitals (green) and onto the  $p$  orbitals with  $m_j = \pm 3/2$  (yellow) respectively. The black range shows the energy range within which we shift the graphene Dirac cone in the respective Gr/TI heterostructures using an electric field. We show the development of the SOC parameters and the orbital decomposition of the Dirac cone states (averaged over a  $k$  range of  $0.04 \text{ \AA}^{-1}$  for  $\text{Bi}_2\text{Te}_3$  and  $0.004 \text{ \AA}^{-1}$  for  $\text{Bi}_2\text{Se}_3$  along the high symmetry path around  $K$ ) during this shifting. For (a) and (b) the horizontal dotted lines indicate the Dirac cone position of an electric field corrected band structure (zero-strain band offset), therefore corresponding to the zooms in the last line of plots in Fig. 4. In the lower plot (“orbital composition”) the black curve shows the general content of TI orbitals in the Dirac cone. The dark-green curve shows how much of that TI content stems from TI  $s$  orbitals. The yellow curve shows how much of the TI  $p$ -orbital content stems from states with quantum number  $m_j = \pm 3/2$ .

phase angle will have a value of  $\Phi = 360^\circ$  at a twist angle of  $\Theta = 30^\circ$ .

The case of the highly commensurate  $\Theta = 30^\circ$  supercell was investigated more closely. We consider the specific shifting configuration hollow, since it is energetically the most favorable. Since its symmetries do not allow for valley-Zeeman SOC, the significant SOC types are Rashba ( $|\lambda_R|$ ) and Kane-Mele ( $\lambda_{KM}$ ). Due to backfolding effects, the Dirac cone coincides with the TI surface state in  $k$  space. Using an electric field, we shift the Dirac cone within a local TI band gap, which results in a change of the sign of  $\lambda_{KM}$ . Furthermore, orbital decomposition considerations reveal that the Dirac cone consists of two distinct alternating types of bands, one

of which obtains its proximity SOC almost exclusively from higher lying bands.

In addition, we show calculations indicating that the effect of lateral shifting is irrelevant for the cases within  $0^\circ \leq \Theta \lesssim 20^\circ$ , while having a strong effect on the highly commensurate  $\Theta = 30^\circ$  supercell.

#### ACKNOWLEDGMENTS

This work was funded by the International Doctorate Program Topological Insulators of the Elite Network of Bavaria, Deutsche Forschungsgemeinschaft SFB 1277 (Grant No. 314695032) and No. SPP 2244 (Grant No. 443416183), and

TABLE III. Parameters extracted from the band structure calculations. For both  $\text{Bi}_2\text{Te}_3$  and  $\text{Bi}_2\text{Se}_3$  and for all angles (except if the band offset is too large and the Dirac cone is shifted into the TI bands), we list the band offset  $\Delta E$  of the Dirac cone with respect to the TI surface band and the extracted model Hamiltonian [Eq. (3)] parameters. The parameters are staggered potential  $\Delta$ , Kane-Mele SOC  $\lambda_{\text{KM}}$ , valley-Zeeman SOC  $\lambda_{\text{VZ}}$ , magnitude of the Rashba SOC  $|\lambda_{\text{R}}|$ , and Rashba angle  $\Phi$ . We denote the offsets and parameters after correction with the electric field with a bar, for example  $\bar{\lambda}_{\text{VZ}}$ . The electric field is defined as positive, if it points from the TI layer to the graphene layer.

$\Theta$ (deg)	$\epsilon$ (%)	$\Phi$ (deg)	$\Delta$ (meV)	$\lambda_{\text{KM}}$ (meV)	$\lambda_{\text{VZ}}$ (meV)	$ \lambda_{\text{R}} $ (meV)	$\Delta E$ (eV)	Electric field (V/nm)	$\bar{\Phi}$ (deg)	$\bar{\Delta}$ (meV)	$\bar{\lambda}_{\text{KM}}$ (meV)	$\bar{\lambda}_{\text{VZ}}$ (meV)	$ \bar{\lambda}_{\text{R}} $ (meV)	$\bar{\Delta E}$ (eV)
<b><math>\text{Bi}_2\text{Te}_3</math></b>														
0	-10.85	180	2.325	0.698	1.256	1.452	0.972	5.554	180	2.257	0.528	0.786	1.037	0.529
0	6.98	180	0.002	-0.004	1.934	0.748	-0.015	-3.399	180	0.037	-0.022	3.026	2.054	0.510
4.3	8.22	152	0.000	-0.006	2.038	0.512	-0.072	-3.838	181	0.034	-0.024	3.126	1.791	0.471
4.7	1.54	146	0.002	-0.003	1.019	0.557	0.141	-2.199	171	-1.936	-0.002	1.254	0.852	0.444
8.9	-3.93	199	0.418	-0.002	-0.319	0.342	0.458	0.247	199	-0.001	0.008	0.050	0.438	0.442
10.9	16.72	19	-0.067	0.271	13.694	7.140	-0.309	-6.171	50	0.109	-0.082	9.562	3.574	0.407
13.9	-1.1	-130	0.010	0.011	-0.464	0.178	0.407	-0.145	-133	0.010	0.006	-0.467	0.183	0.418
17.5	8.22	-10	0.001	0.154	3.513	2.897	-0.044	-3.624	54	0.014	-0.028	-1.568	0.531	0.458
19.1	1.08	-42	-0.001	0.024	-0.814	0.980	0.114	-2.406	-45	-0.001	0.005	-1.320	0.143	0.114
19.1	17.93						-0.393	-5.656	59	-0.034	-0.035	8.578	7.467	0.396
19.1	-5.66						0.772	1.797	-48	0.007	0.006	-2.720	0.636	0.427
30	2.94		0.000	-12.400	0.000	5.089	0.255	-0.771		0.000	-8.413	0.000	2.703	0.324
<b><math>\text{Bi}_2\text{Se}_3</math></b>														
0	-15.79	180	1.496	0.252	0.726	0.816	1.423							
0	1.05	180	0.002	-0.007	1.217	0.901	0.704	0.074	180	0.003	-0.007	1.204	0.881	0.692
4.3	2.22	-178	-0.001	-0.006	1.195	0.621	0.518	-1.36	-175	0.004	-0.010	1.344	0.879	0.695
4.7	-4.09	190	0.001	-0.005	0.381	0.616	0.831	1.05	-174	-0.001	0.000	0.369	0.447	0.592
10.9	10.25	47	-0.049	0.002	3.175	1.024	0.240	-4.114	56	0.054	-0.018	5.016	1.554	0.644
13.9	-6.58	-155	0.004	0.007	-0.496	0.623	0.982	2.216	-148	0.003	0.004	-0.331	0.330	0.664
17.5	2.22	17	0.080	0.027	-0.552	0.076	0.519	-1.354	-150	0.006	-0.017	-1.490	0.281	0.692
19.1	11.4	47	0.035	0.006	2.304	2.217	0.225	-3.624	53	0.003	-0.035	3.197	3.146	0.622
19.1	-4.52	-120	0.005	0.002	-0.917	0.299	0.682	-0.098	-124	0.000	0.000	-0.935	0.315	0.706
20.8	-0.17	-41	0.001	-0.007	-1.258	0.468	0.524	-1.313	-85	-0.008	-0.031	-2.194	0.819	0.669
21.1	4.78	23	0.022	-0.028	0.600	1.680	0.388	-2.36	23	-0.005	-0.074	0.844	2.809	0.632
30	-2.77		0.000	0.517	0.000	1.340	0.754	0.617		0.000	0.049	0.000	1.091	0.700

the European Union Horizon 2020 Research and Innovation Program under Grant No. 881603 (Graphene Flagship) and Flagera project 2DSOTECH.

**APPENDIX A: COMPUTATIONAL DETAILS**

All electronic structure calculations are performed implementing density functional theory (DFT) [60] using QUANTUM ESPRESSO [61]. Self-consistent calculations are carried out with a  $k$  point sampling of  $n_k \times n_k \times 1$ . The number  $n_k$  is listed in Table IV for all cases. We use charge density cutoffs  $E_\rho = 480\text{Ry}$  and wave function kinetic cutoff  $E_{\text{WFC}} = 48\text{Ry}$  ( $E_{\text{WFC}} = 58\text{Ry}$  for  $\text{Bi}_2\text{Se}_3$ ) for the fully relativistic pseudopotential with the projector augmented wave method [62] with the Perdew-Burke-Ernzerhof exchange correlation functional [63]. Graphene's  $d$  orbitals are not included in the calculations. We used Grimme D-2 van der Waals corrections [64–66].

The electric fields are implemented in the DFT calculations using a sawtooth potential in  $z$  direction within the quasi-two-dimensional unit cell. The electric potential increases linearly in the area of the heterostructure and then falls rapidly in the vacuum.

TABLE IV. Computational details:  $k$  grid density (we used a  $n_k \times n_k$  grid) for all calculations.

	$(n, m)$	$(n', m')$	$n_k$ (1QL)	$n_k$ (3QL)
0.0°	(0 2)	(0 1)	15	
0.0°	(0 5)	(0 3)	6	
4.3°	(2 3)	(1 2)	9	3
4.7°	(4 3)	(2 2)	3	
8.9°	(1 5)	(0 3)	3	
10.9°	(2 1)	(1 1)	15	9
13.9°	(1 3)	(0 2)	15	9
16.1°	(3 1)	(1 1)	15	
17.5°	(3 2)	(1 2)	9	3
19.1°	(4 0)	(2 1)	12	
19.1°	(5 0)	(2 1)	6	
19.1°	(2 4)	(0 3)	3	
19.1°	(2 4)	(0 3)	3	
20.8°	(4 3)	(1 3)	3	
21.1°	(5 1)	(2 2)	3	
21.8°	(4 2)	(1 2)	6	
30.0°	(1 1)	(0 1)	45	45
30.0°	(7 0)	(2 2)	3	

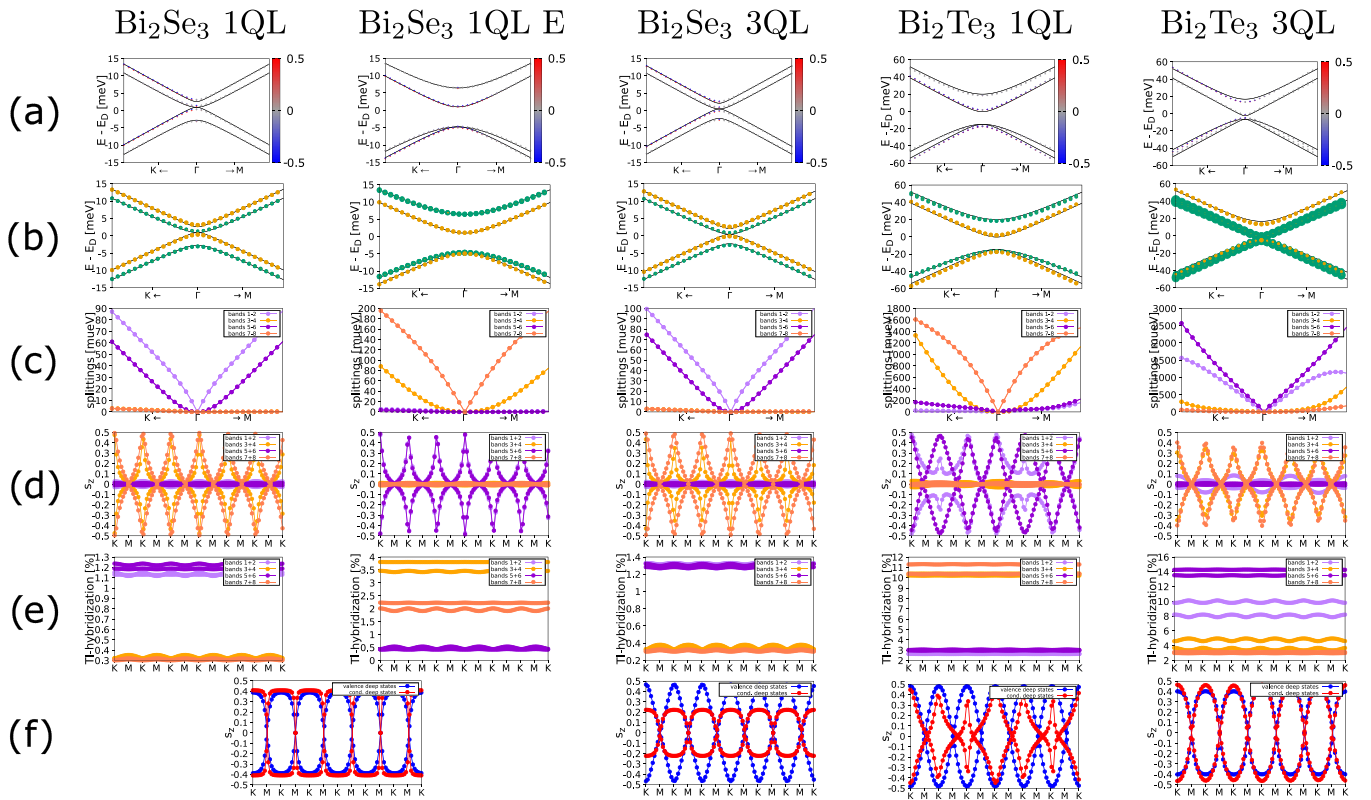


FIG. 7. The two types of band pairs of the eight band Dirac cone for  $\Theta = 30^\circ$ . For selected cases we show the Dirac cone and the distinct properties of the two types of band pairs it consists of. All cases are without applied electric field “ $\text{Bi}_2\text{Se}_3$  1Q E,” where an electric field of 4.11 V/nm was applied. (a, b) Dirac cone, with color coded spin  $z$  (a) and color coded orbital decomposition (b). In (b) green dots show TI  $s$ -orbital contribution, while yellow dots shows  $m_j = \pm 3/2$  orbital contribution as in Fig. 6. Line (c) shows the ( $\mu\text{eV}$ ) splittings of the band pairs, where “bands 1–2” refers to the energetically lowest pair of bands. All following lines (d–f) are concerned with the properties along a circular path around the Dirac cone at 55 meV. (d, e) Spin  $z$  expectation values and the contribution of the TI orbitals along this circular path respectively. (f) Like (d) the spin  $z$  along the circular path, but not for the Dirac cone, but for selected deep lying TI states with major  $m_j = \pm 3/2$  contribution (see Fig. 6). The labels “K” and “M” in (d)–(f) indicate that the  $k$  point is lying on the  $\Gamma K$  (or the  $\Gamma M$ ) connection line.

## APPENDIX B: DISTINGUISHING THE TWO TYPES OF BAND PAIRS FOR $\Theta = 30^\circ$

In the main paper we touched on the two different kinds of band pairs of the Dirac cones in the case of the  $\Theta = 30^\circ$  supercell band structures. We now explore this in detail. In the following we will call band pairs type 1, if they have similar properties as the energetically lowest pair of bands in the  $\text{Bi}_2\text{Se}_3$  1QL case without electric field (Fig. 7, first column). Accordingly, type 2 band pairs then are similar to the band pair energetically above this type 1 case. Figure 7 summarizes the relevant differences of the two types. From Figs. 7(a) and 7(d) we see that the spin- $z$  expectation values of type 1 bands are (almost) zero: both bands are unpolarized in the  $z$  direction. In contrast, type 2 band pairs show an anisotropic spin structure, where the bands show opposite spin- $z$  values along the  $\Gamma K$  line and vanishing values along the  $\Gamma M$  line. Additionally, the in-plane spin structures we see in Fig. 4 are also bound to the type of band pair. Figure 7(b) shows that type 1 band pairs have relevant contributions from TI  $m_j = \pm 3/2$  states, while type 2 band pairs have relevant contributions from TI  $s$ -orbital contributions. In Fig. 7(c), we show the splittings within the band pairs: Although both type 1

and type 2 bands are only split on the  $\mu\text{eV}$  scale, the splittings of type 1 bands are significantly higher and increase to the meV range, when moving away from the center of the Dirac cone at  $\Gamma$ . This splitting is enough to overcome the small spin splitting, seen in type 2 bands. In Fig. 7(e), one can see that the TI content of type 1 band pairs is higher than that of type 2 band pairs by a factor of about 5 on average. Finally, in Fig. 7(f) we see that the same spin structure seen in type 2 bands can be seen in deep lying (so energetically low valence or energetically high conduction) bands of the TI. We conclude that on the one hand type 1 bands acquire their proximity SOC almost exclusively from deep lying TI states imprinting their spin- $z$  structure and their  $m_j = \pm 3/2$  character. Type 2 band pairs on the hand acquire the majority of their proximity SOC from the near surface state, which results in a larger splitting destroying the spin- $z$  structure and a significant TI  $s$ -orbital content. Comparing the different cases, we see that different structures can entail a different ordering of type 1 and type 2 bands. Shifting the Dirac cone within the TI band structure can result in a switch of this ordering as well. In fact, we observe such a switching of the ordering by electric field for all of the cases in Fig. 6, except 3QL of  $\text{Bi}_2\text{Se}_3$ .

### APPENDIX C: ALTERNATIVE FITTING HAMILTONIAN FOR $\Theta = 30^\circ$

The Dirac cone of the hollow  $\Theta = 30^\circ$  supercell has an intricate spin structure (see Fig. 7). In the main paper we neglect this fine structure, since it is based on  $\mu\text{eV}$  splittings within the band pairs. Now, we try to describe this fine structure using a full tight binding Hamiltonian akin to the one used in Ref. [31]:

$$\begin{aligned}
 H = & \sum_{\alpha=0,p} t_\alpha \sum_{\langle\langle ij \rangle\rangle, s} c_{is}^\dagger c_{js} + \sum_{i,s} \Delta_i c_{is}^\dagger c_{is} \\
 & + \frac{i}{3\sqrt{3}} \sum_{\langle\langle ij \rangle\rangle, ss'} c_{is}^\dagger c_{js'} (\lambda_{KM,2} + \xi \lambda_{VZ}) [v_{ij} s_z]_{ss'} \\
 & + \frac{2i}{3} \sum_{\langle ij \rangle, ss'} c_{is}^\dagger c_{js'} [(\lambda_R \hat{\mathbf{z}} + \lambda_{R,2} \boldsymbol{\rho}) \cdot (\mathbf{s} \times \mathbf{d}_{ij})]_{ss'}. \quad (\text{C1})
 \end{aligned}$$

The single brackets constitute sums over nearest neighbors and the double brackets constitute sums over next nearest neighbors.  $c_{is}^\dagger$  and  $c_{is}$  are the creation and annihilation operators of an electron at site  $i$  with spin  $s$ ,  $\mathbf{d}_{i,j}$  is a unit vector pointing from site  $j$  to nearest neighbor site  $i$ ,  $\mathbf{s}$  is a vector containing the Pauli matrices,  $v_{ij}$  is equal to  $+1$  for clockwise and equal to  $-1$  for counterclockwise hoppings from site  $j$  to  $i$ ,  $\xi$  is  $+1$  for sublattice  $A$  and  $-1$  for sublattice  $B$ ,  $\hat{\mathbf{z}}$  is the unit vector in  $z$  direction, and  $\boldsymbol{\rho}$  is an in-plane vector representing the electric fields in Fig. 8(a). The first term of  $H$  describes the orbital part with  $t_0$  as (stronger) hopping within the carbon ring depicted in Fig. 8(a) and  $t_p$  as the (weaker) hopping parameter between such carbon rings. This makes  $t_0 - t_p$  the Kekule distortion parameter. The second term describes a series of onsite potentials  $\Delta_i$ , which are only used in the fitting of the top case. The third term describes Kane-Mele and valley-Zeeman SOC. Note that this term is an exact translation of the Kane-Mele and valley-Zeeman terms in Eq. (5) in contrast to Ref. [31], where the Kane-Mele hoppings only exist on the central carbon ring. The fourth term describes a Rashba SOC related to an electric field in  $z$  direction [again an exact translation of the term in Eq. (6)] and an additional Rashba term  $\lambda_{R,2}$  related to electric fields  $\boldsymbol{\rho}$  depicted as arrows in Fig. 8(a). The electric fields are all pointing inward to the carbon ring located under the Se (or Te) atom closest to graphene. There are two distinct types of arrows: to one we assign  $|\boldsymbol{\rho}| = 1$  [large arrows in Fig. 8(a)], to the other  $|\boldsymbol{\rho}| = 0.2$  [small arrows in Fig. 8(a)]. Note that Ref. [31] does not allow for the in-plane Rashba connected to the smaller arrows.

For the hollow case as in the paper we have  $\lambda_{VZ} = \Delta_i = 0$ . We obtain good fits only for very small but nonzero values for  $|\lambda_R|$  and therefore simply fix it to  $|\lambda_R| = 0.01$  meV for all fits. The remaining parameters therefore are  $\lambda_{KM,2}$ ,  $t_0 - t_p$ , and  $\lambda_{R,2}$ . The general spin- $z$  structure of the type 2  $\Theta = 30^\circ$  band pairs can be modeled with the fittings [see Fig. 8(b)]. To model the spin- $z$  structure of a type 1 band pair, one can simply set the magnitude of all in-plane electric fields to equal values  $|\boldsymbol{\rho}| = 0.6$  for the directions indicated by both the large and the small arrows. This will not significantly change the values of the other fitting parameters. Note that the in-plane

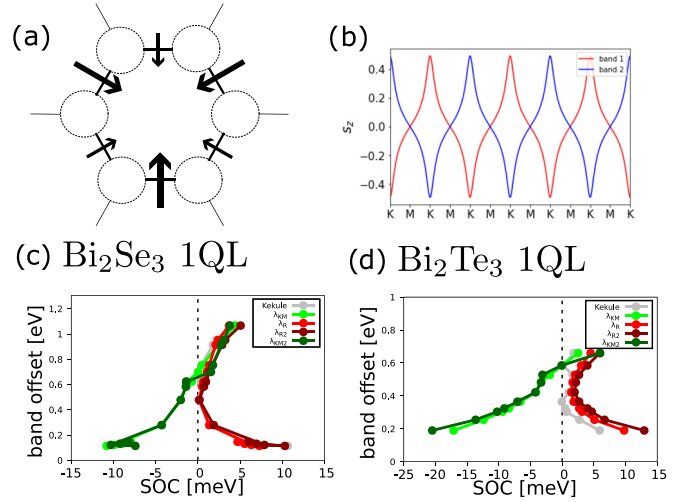


FIG. 8. Alternative fitting results. (a) Schematic of the additional fitting parameters  $\lambda_{R,2}$  and  $t_0 - t_p$  introducing an in-plane Rashba effect and a Kekule distortion effect. The carbon ring beneath the Se (or Te) atom closest to the graphene plane is shown. The electric field producing the in-plane Rashba effect is depicted by arrows, and the electric field along the smaller arrows is set to be only 20% compared to the one along the larger arrows. The thicker connection lines between the carbon atoms indicate increased hoppings by the Kekule distortion. (b) Exemplary ( $\text{Bi}_2\text{Se}_3$  1QL, without electric field correction) spin- $z$  structure along a circle at  $\approx 60$  meV above the Dirac cone. The labels “K” and “M” indicate that the  $k$  point is lying on the  $\Gamma K$  (or the  $\Gamma M$ ) connection line. (c, d) SOC parameters  $|\lambda_R|$  and  $\lambda_{KM}$  [extracted with Eq. (3), see Fig. 6] in comparison with the parameters  $\lambda_{R,2}$ ,  $\lambda_{KM,2}$ , and  $t_0 - t_p$  [extracted with Eq. (C1)] for different electric fields. The electric field range used to shift the graphene Dirac cone within the TI bands is the same as in Fig. 6.

spin structure also cannot be sufficiently reproduced using this Hamiltonian.

We show the fittings results in Figs. 8(c) and 8(d) for  $\text{Bi}_2\text{Se}_3$  and  $\text{Bi}_2\text{Te}_3$  respectively for the same electric fields as in Fig. 6. We see the same results for Kane-Mele SOC (compare light green to dark green curve). Also the new in-plane Rashba SOC replaces the out-of-plane Rashba SOC (compare red to dark-red curve). The Kekule distortion parameter will follow a similar behavior as the Rashba SOC increasing drastically in the vicinity of a TI band.

### APPENDIX D: EFFECT OF LATERAL SHIFTING

For incommensurate heterostructures the lateral shifting degree of freedom does not play a role. Assuming a sample infinite in  $x$  and  $y$  direction, every shifting configuration exists somewhere on the sample. The physical properties of the configurations will then average out, when considering the properties of the whole material. However, the structures used in our DFT calculations are commensurate to be computationally viable and the lattice constants are forced by strain to be compatible. Therefore, different lateral relative shifts might ensue different physical properties including different proximity induced SOC.

Naturally, this effect is less relevant for large supercells, for which an averaging over the different shifts will occur within

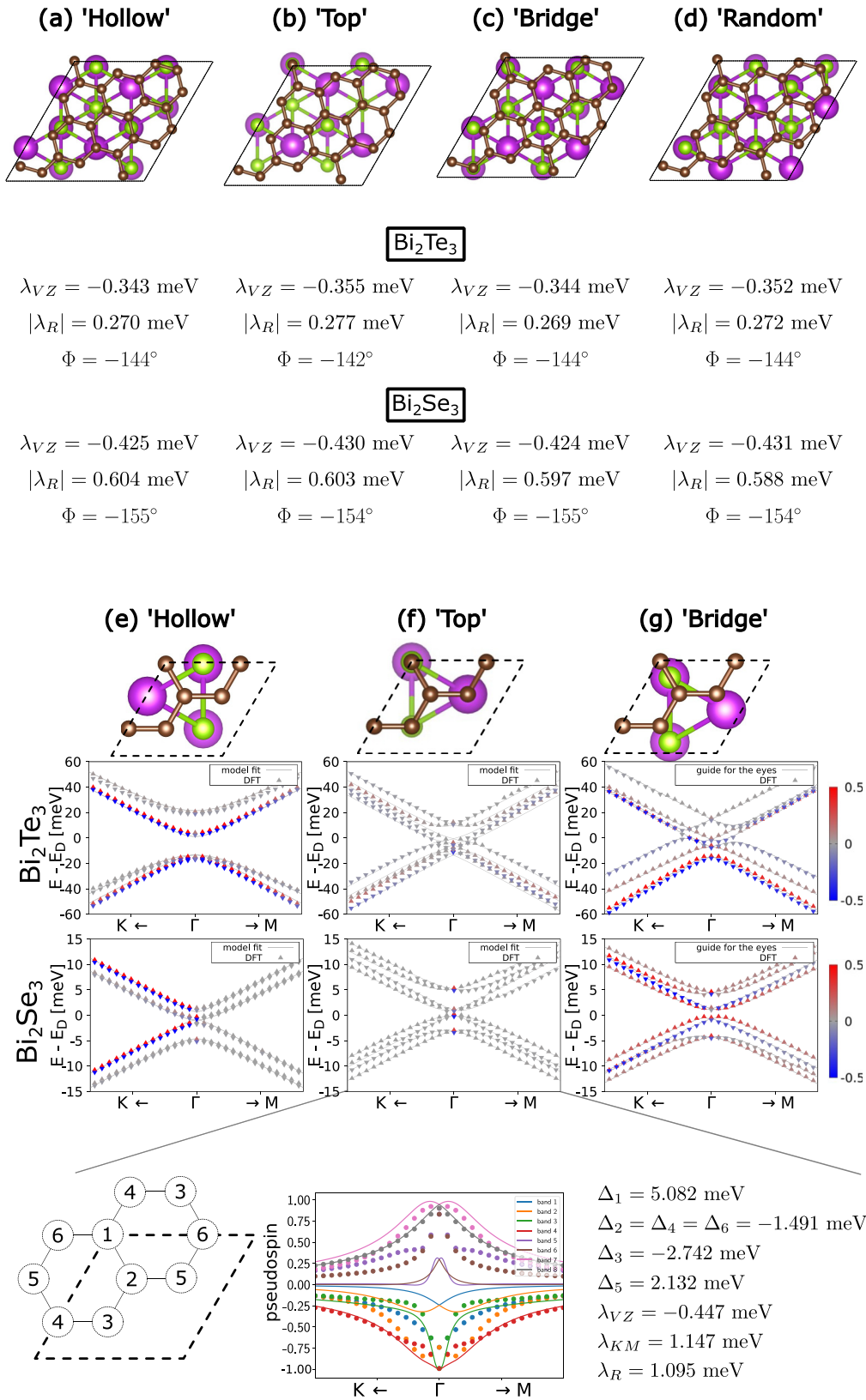


FIG. 9. Supercells with different lateral shifting positions for (a–d)  $\Theta = 13.9^\circ$  and (e–g)  $\Theta = 30^\circ$ . For the former, we list the relevant extracted SOC parameters  $|\lambda_R|$ ,  $\lambda_{VZ}$ , and  $\Phi$  for both Gr/Bi<sub>2</sub>Te<sub>3</sub> and Gr/Bi<sub>2</sub>Se<sub>3</sub>. For the latter we show the proximity SOC modified Dirac cone band structure with color coded spin  $z$ . The triangles represent DFT data. For the cases where satisfactory fittings were possible [(e) and (f)] the gray lines represent the energies of the fit, while for (g) the gray lines represent only a guide to the eyes connecting the data points of the same band. For the top case of Gr/Bi<sub>2</sub>Se<sub>3</sub> we additionally present the fitting results of the pseudospin and the extracted fitting parameters. The sketch on the left shows the labeling of the atoms in the top case.

TABLE V. Comparison between extracted SOC parameters for selected cases between structures with 1QL thick TI slabs and 3QL thick TI slabs. The parameters are extracted from calculations without electric field corrections.

Thickness	$\Theta$ (deg)	$\lambda_{KM}$ (meV)	$\lambda_{VZ}$ (meV)	$ \lambda_R $ (meV)	$\Phi$ (deg)
Bi <sub>2</sub> Te <sub>3</sub>					
1QL	4.3	-0.01	2.04	0.52	152
3QL	4.3	0.01	1.65	0.50	79
1QL	13.9	0.01	-0.46	0.18	-130
3QL	13.9	0.01	-0.36	0.28	-142
1QL	17.5	0.16	3.51	2.90	-10
3QL	17.5	0.08	3.35	2.06	-25
Bi <sub>2</sub> Se <sub>3</sub>					
1QL	4.3	-0.01	1.19	0.62	-178
3QL	4.3	0.00	1.10	0.38	171
1QL	10.9	0.01	3.18	1.02	47
3QL	10.9	0.01	3.24	1.00	46
1QL	13.9	0.01	-0.50	0.62	-155
3QL	13.9	0.00	-0.43	0.60	-154
1QL	17.5	0.03	-0.55	0.08	17
3QL	17.5	-0.00	0.02	0.32	23

the supercell. We show this by investigating the shifting dependence for two supercells: the 13.9° and the 30° supercell. While the former consists of a total of 46 atoms and gives enough area for the different configurations to average out, the latter only consists of 13 atoms. Therefore, different lateral shifting positions will lead to different effects on the Dirac cone for the 30° supercell.

We defined four different shifting options: hollow, top, bridge, and “random,” which we show in Fig. 9. The keywords indicate how the Te atom closest to the graphene layer is positioned with respect to the graphene structure. For the 30° case there is only one such atom per unit cell, while for the 13.9° supercell there are multiple ones, with different positions (we describe the one closest to the corner of the supercell). Therefore, in the 13.9° case, the Dirac cones for the different shifting positions look almost the same, as the extracted fitting parameters show hardly any difference. In contrast, the Dirac cone of the 30° case varies widely depending on the lateral shift.

We now focus on the 30° supercell. Since the hollow configuration is the energetically most favorable and has the simplest band structure, we focus on it in the main paper. Additionally, we fitted the Dirac cone of the top case to a full tight binding Hamiltonian, since the simple model Hamiltonian [Eq. (3)] in the main paper is not able to capture the features

of the band structure, which come from the specific shifting position with respect to the  $\sqrt{3} \times \sqrt{3}$  graphene supercell. By using the same SOC parameters  $\lambda_{VZ}$ ,  $\lambda_{KM}$ , and  $|\lambda_R|$  and additionally extending the sublattice imbalance  $\Delta$  to a general onsite potential  $\bar{\Delta}$  [see Eq. (C1)] for the six carbon atoms, we were able to describe the Dirac cone of the top configuration reasonably well (see Fig. 9). For all eight bands, the spin- $z$  expectation values are zero, while the pseudospin shows an intricate structure. For the bridge case, we were not able to find satisfying fitting parameters.

#### APPENDIX E: EFFECT OF INCREASED THICKNESS OF THE TI SLAB

Varying the thickness of the TI layer changes its band structure. When increasing the number of QLs, one can see the TI surface state at  $\Gamma$  fully forming. While for 1QL the overlap between the upper and lower surface states opens a large gap, the surface states of the 3QL case are spatially separated enough for the characteristic linear sloped surface state to arise. Since the graphene Dirac cone of the  $\Theta = 30^\circ$  supercell interacts directly with the TI surface state, it will be affected significantly by the exact form of the surface state and therefore by the thickness of the TI.

But also, for the other twist angles, a dependency on the TI thickness is not excluded, since also the TI bands away from  $\Gamma$  are influenced by this change which can in turn then change the proximity SOC. To investigate this, we calculated the band structures for the 3QL cases of some of our supercells and gather the extracted parameters in Table V. Note that we compare the results without electric field corrected band offsets, because the 3QL TI band structure is significantly more susceptible to unwanted distortion by the electric field. However, since we are only comparing the 1QL case with the 3QL case, which both have the same strain, using the parameters from the uncorrected calculations is a valid approach. The table shows that while in most of the scenarios the SOC is not strongly affected by the TI thickness, there are two cases highlighting the importance of the TI thickness.

(1) For the Gr/Bi<sub>2</sub>Te<sub>3</sub>  $\Theta = 4.3^\circ$  supercell, the change from 1QL to 3QL changes the Rashba phase angle by a significant amount from 152° to only 79°.

(2) For the Gr/Bi<sub>2</sub>Se<sub>3</sub>  $\Theta = 17.5^\circ$  supercell, the 1QL case is dominated by valley-Zeeman type SOC  $\lambda_{VZ}$ , while in the 3QL case the Rashba type SOC  $|\lambda_R|$  is dominating. Here, the vicinity to the TI surface state in  $k$  space might already be a reason for this massive change in proximity SOC.

In conclusion, we see that for  $0^\circ < \Theta \lesssim 20^\circ$  the proximity SOC dependency on the TI thickness is overall not too large, but should not fully be neglected.

- [1] S. Singh, J. Katoch, J. Xu, C. Tan, T. Zhu, W. Amamou, J. Hone, and R. Kawakami, Nanosecond spin relaxation times in single layer graphene spin valves with hexagonal boron nitride tunnel barriers, *Appl. Phys. Lett.* **109**, 122411 (2016).
- [2] M. Drögeler, C. Franzen, F. Volmer, T. Pohlmann, L. Banszerus, M. Wolter, K. Watanabe, T. Taniguchi, C. Stampfer, and B.

Beschoten, Spin lifetimes exceeding 12 ns in graphene nonlocal spin valve devices, *Nano Lett.* **16**, 3533 (2016).

- [3] K.I. Bolotin, K.J. Sikes, Z. Jiang, M. Klima, G. Fudenberg, J. Hone, P. Kim, and H. L. Stormer, Ultrahigh electron mobility in suspended graphene, *Solid State Commun.* **146**, 351 (2008).

- [4] X. Du, I. Skachko, A. Barker, and E. Y. Andrei, Approaching ballistic transport in suspended graphene, *Nat. Nanotechnol.* **3**, 491 (2008).
- [5] C. L. Kane and E. J. Mele, Quantum Spin Hall Effect in Graphene, *Phys. Rev. Lett.* **95**, 226801 (2005).
- [6] C. L. Kane and E. J. Mele,  $\mathbb{Z}_2$  Topological Order and the Quantum Spin Hall Effect, *Phys. Rev. Lett.* **95**, 146802 (2005).
- [7] Z. Qiao, S. A. Yang, W. Feng, W.-K. Tse, J. Ding, Y. Yao, J. Wang, and Q. Niu, Quantum anomalous Hall effect in graphene from Rashba and exchange effects, *Phys. Rev. B* **82**, 161414(R) (2010).
- [8] Y. Ren, Z. Qiao, and Q. Niu, Topological phases in two-dimensional materials: A review, *Rep. Prog. Phys.* **79**, 066501 (2016).
- [9] T. Frank, P. Högl, M. Gmitra, D. Kochan, and J. Fabian, Protected Pseudohelical Edge States in  $\mathbb{Z}_2$ -Trivial Proximitized Graphene, *Phys. Rev. Lett.* **120**, 156402 (2018).
- [10] P. Högl, T. Frank, K. Zollner, D. Kochan, M. Gmitra, and J. Fabian, Quantum Anomalous Hall Effects in Graphene from Proximity-Induced Uniform and Staggered Spin-Orbit and Exchange Coupling, *Phys. Rev. Lett.* **124**, 136403 (2020).
- [11] J. Y. Khoo, A. F. Morpurgo, and L. Levitov, On-demand spin-orbit interaction from which-layer tunability in bilayer graphene, *Nano Lett.* **17**, 7003 (2017).
- [12] M. Gmitra and J. Fabian, Proximity Effects in Bilayer Graphene on Monolayer  $\text{WSe}_2$ : Field-Effect Spin Valley Locking, Spin-Orbit Valve, and Spin Transistor, *Phys. Rev. Lett.* **119**, 146401 (2017).
- [13] J. O. Island, X. Cui, C. Lewandowski, J. Y. Khoo, E. M. Spanton, H. Zhou, D. Rhodes, J. C. Hone, T. Taniguchi, K. Watanabe, L. S. Levitov, M. P. Zaletel, and A. F. Young, Spinorbit-driven band inversion in bilayer graphene by the van der Waals proximity effect, *Nature (London)* **571**, 85 (2019).
- [14] P. Tiwari, S. K. Srivastav, and A. Bid, Electric-Field-Tunable Valley Zeeman Effect in Bilayer Graphene Heterostructures: Realization of the Spin-Orbit Valve Effect, *Phys. Rev. Lett.* **126**, 096801 (2021).
- [15] J. Amann, T. Völkl, D. Kochan, K. Watanabe, T. Taniguchi, J. Fabian, D. Weiss, and J. Eroms, Gate-tunable spin-orbit-coupling in bilayer graphene- $\text{WSe}_2$ -heterostructures, *Phys. Rev. B* **105**, 115425 (2022).
- [16] S. Zihlmann, A. W. Cummings, J. H. Garcia, M. Kedves, K. Watanabe, T. Taniguchi, C. Schönenberger, and P. Makk, Large spin relaxation anisotropy and valley-zeeman spin-orbit coupling in  $\text{WSe}_2$ /graphene/ $h$ -bn heterostructures, *Phys. Rev. B* **97**, 075434 (2018).
- [17] A. W. Cummings, J. H. Garcia, J. Fabian, and S. Roche, Giant Spin Lifetime Anisotropy in Graphene Induced by Proximity Effects, *Phys. Rev. Lett.* **119**, 206601 (2017).
- [18] T. S. Ghiasi, J. Ingla-Aynés, A. A. Kaverzin, and B. J. Van Wees, Large Proximity-Induced Spin Lifetime Anisotropy in Transition-Metal Dichalcogenide/Graphene Heterostructures, *Nano Lett.* **17**, 7528 (2017).
- [19] B. Zhao, B. Karpiak, D. Khokhriakov, A. Johansson, A. Md. Hoque, X. Xu, Y. Jiang, I. Mertig, and S. P. Dash, Unconventional charge spin conversion in Weyl-semimetal  $\text{WTe}_2$ , *Adv. Mater.* **32**, 2000818 (2020).
- [20] J. Ingla-Aynés, I. Groen, F. Herling, N. Ontoso, C. K. Safer, F. de Juan, L. E. Hueso, M. Gobbi, and F. Casanova, Omnidirectional spin-to-charge conversion in graphene/ $\text{NbSe}_2$  van der Waals heterostructures, *2D Mater.* **9**, 045001 (2022).
- [21] C. G. Péterfalvi, A. David, P. Rakyta, G. Burkard, and A. Kormányos, Quantum interference tuning of spin-orbit coupling in twisted van der Waals trilayers, *Phys. Rev. Res.* **4**, L022049 (2022).
- [22] A. Veneri, D. T. S. Perkins, C. G. Péterfalvi, and A. Ferreira, Twist angle controlled collinear Edelstein effect in van der Waals heterostructures, *Phys. Rev. B* **106**, L081406 (2022).
- [23] S. Lee, D. J. P. de Sousa, Y.-K. Kwon, F. de Juan, Z. Chi, F. Casanova, and T. Low, Charge-to-spin conversion in twisted graphene/ $\text{WSe}_2$  heterostructures, *Phys. Rev. B* **106**, 165420 (2022).
- [24] A. K. Geim and I. V. Grigorieva, Van der Waals heterostructures, *Nature (London)* **499**, 419 (2013).
- [25] D. L. Duong, S. J. Yun, and Y. H. Lee, Van der Waals Layered Materials: Opportunities and Challenges, *ACS Nano* **11**, 11803 (2017).
- [26] M. Gmitra and J. Fabian, Graphene on transition-metal dichalcogenides: A platform for proximity spin-orbit physics and optospintronics, *Phys. Rev. B* **92**, 155403 (2015).
- [27] M. Gmitra, D. Kochan, P. Högl, and J. Fabian, Trivial and inverted dirac bands and the emergence of quantum spin hall states in graphene on transition-metal dichalcogenides, *Phys. Rev. B* **93**, 155104 (2016).
- [28] T. Frank, S. Irmer, M. Gmitra, D. Kochan, and J. Fabian, Copper adatoms on graphene: Theory of orbital and spin-orbital effects, *Phys. Rev. B* **95**, 035402 (2017).
- [29] Z. Wang, D.-K. Ki, H. Chen, H. Berger, A. H. MacDonald, and A. F. Morpurgo, Strong interface-induced spin-orbit interaction in graphene on  $\text{WS}_2$ , *Nat. Commun.* **6**, 8339 (2015).
- [30] A. Avsar, J. Y. Tan, T. Taychatanapat, J. Balakrishnan, G. K. W. Koon, Y. Yeo, J. Lahiri, A. Carvalho, A. S. Rodin, E. C. T. O'Farrell, G. Eda, A. H. Castro Neto, and B. Özyilmaz, Spin-orbit proximity effect in graphene, *Nat. Commun.* **5**, 4875 (2014).
- [31] K. Song, D. Soriano, A. W. Cummings, R. Robles, P. Ordejón, and S. Roche, Spin proximity effects in graphene/topological insulator heterostructures, *Nano Lett.* **18**, 2033 (2018).
- [32] K. Zollner and J. Fabian, Single and bilayer graphene on the topological insulator  $\text{Bi}_2\text{Se}_3$ : Electronic and spin-orbit properties from first principles, *Phys. Rev. B* **100**, 165141 (2019).
- [33] S. Jafarpisheh, A. W. Cummings, K. Watanabe, T. Taniguchi, B. Beschoten, and C. Stampfer, Proximity-induced spin-orbit coupling in graphene/ $\text{Bi}_{1.5}\text{Sb}_{0.5}\text{Te}_{1.7}\text{Se}_{1.3}$  heterostructures, *Phys. Rev. B* **98**, 241402(R) (2018).
- [34] D. Khokhriakov, A. W. Cummings, K. Song, M. Vila, B. Karpiak, A. É. Dankert, S. Roche, and S. P. Dash, Tailoring emergent spin phenomena in Dirac material heterostructures, *Sci. Adv.* **4**, eaat9349 (2018).
- [35] H. Steinberg, L. A. Orona, V. Fatemi, J. D. Sanchez-Yamagishi, K. Watanabe, T. Taniguchi, and P. Jarillo-Herrero, Tunneling in graphene-topological insulator hybrid devices, *Phys. Rev. B* **92**, 241409(R) (2015).
- [36] A. Zalic, T. Dvir, and H. Steinberg, High-density carriers at a strongly coupled interface between graphene and a three-dimensional topological insulator, *Phys. Rev. B* **96**, 075104 (2017).

- [37] S. Rajput, Y.-Y. Li, M. Weinert, and L. Li, Indirect interlayer bonding in graphene-topological insulator van der Waals heterostructure: Giant spinorbit splitting of the graphene dirac states, *ACS Nano* **10**, 8450 (2016).
- [38] W. Dang, H. Peng, H. Li, P. Wang, and Z. Liu, Epitaxial heterostructures of ultrathin topological insulator nanoplate and graphene, *Nano Lett.* **10**, 2870 (2010).
- [39] P. Lee, K.-H. Jin, S. J. Sung, J. G. Kim, M.-T. Ryu, H.-M. Park, S.-H. Jhi, N. Kim, Y. Kim, S. Uk Yu, K. S. Kim, D. Y. Noh, and J. Chung, Proximity effect induced electronic properties of graphene on  $\text{Bi}_2\text{Te}_2\text{Se}$ , *ACS Nano* **9**, 10861 (2015).
- [40] J. Kiemle, L. Powalla, K. Polyudov, L. Gulati, M. Singh, A. W. Holleitner, M. Burghard, and C. Kastl, Gate-tunable helical currents in commensurate topological insulator/graphene heterostructures, *ACS Nano* **16**, 12338 (2022).
- [41] C.-L. Song, Y.-L. Wang, Y.-P. Jiang, Y. Zhang, C.-Z. Chang, L. Wang, K. He, X. Chen, J.-F. Jia, Y. Wang, Z. Fang, X. Dai, X.-C. Xie, X.-L. Qi, S.-C. Zhang, Q.-K. Xue, and X. Ma, Topological insulator  $\text{Bi}_2\text{Se}_3$  thin films grown on double-layer graphene by molecular beam epitaxy, *Appl. Phys. Lett.* **97**, 143118 (2010).
- [42] J. Zhang, C. Triola, and E. Rossi, Proximity Effect in Graphene-Topological-Insulator Heterostructures, *Phys. Rev. Lett.* **112**, 096802 (2014).
- [43] C. De Beule, M. Zarenia, and B. Partoens, Transmission in graphene-topological insulator heterostructures, *Phys. Rev. B* **95**, 115424 (2017).
- [44] W. Cao, R.-X. Zhang, P. Tang, G. Yang, J. Sofo, W. Duan, and C.-X. Liu, Heavy dirac fermions in a graphene/topological insulator hetero-junction, *2D Mater.* **3**, 034006 (2016).
- [45] K.-H. Jin and S.-H. Jhi, Proximity-induced giant spin-orbit interaction in epitaxial graphene on a topological insulator, *Phys. Rev. B* **87**, 075442 (2013).
- [46] Z. Lin, W. Qin, J. Zeng, W. Chen, P. Cui, J.-H. Cho, Z. Qiao, and Z. Zhang, Competing gap opening mechanisms of monolayer graphene and graphene nanoribbons on strong topological insulators, *Nano Lett.* **17**, 4013 (2017).
- [47] W. Liu, X. Peng, X. Wei, H. Yang, G. M. Stocks, and J. Zhong, Surface and substrate induced effects on thin films of the topological insulators  $\text{Bi}_2\text{Se}_3$  and  $\text{Bi}_2\text{Te}_3$ , *Phys. Rev. B* **87**, 205315 (2013).
- [48] I. Popov, M. Mantega, A. Narayan, and S. Sanvito, Proximity-induced topological state in graphene, *Phys. Rev. B* **90**, 035418 (2014).
- [49] T. Naimer, K. Zollner, M. Gmitra, and J. Fabian, Twist-angle dependent proximity induced spin-orbit coupling in graphene/transition metal dichalcogenide heterostructures, *Phys. Rev. B* **104**, 195156 (2021).
- [50] M. Koshino, Interlayer interaction in general incommensurate atomic layers, *New J. Phys.* **17**, 015014 (2015).
- [51] S. Nakajima, The crystal structure of  $\text{Bi}_2\text{Te}_{3-x}\text{Se}_x$ , *J. Phys. Chem. Solids* **24**, 479 (1963).
- [52] D. S. Koda, F. Bechstedt, M. Marques, and L. K. Teles, Coincidence lattices of 2D crystals: Heterostructure predictions and applications, *J. Phys. Chem. C* **120**, 10895 (2016).
- [53] S. Carr, S. Fang, and E. Kaxiras, Electronic-structure methods for twisted moiré layers, *Nat. Rev. Mater.* **5**, 748 (2020).
- [54] C. Si, Z. Sun, and F. Liu, Strain engineering of graphene: A review, *Nanoscale* **8**, 3207 (2016).
- [55] S.-M. Choi, S.-H. Jhi, and Y.-W. Son, Effects of strain on electronic properties of graphene, *Phys. Rev. B* **81**, 081407(R) (2010).
- [56] S. R. Bahn and K. W. Jacobsen, An object-oriented scripting interface to a legacy electronic structure code, *Comput. Sci. Eng.* **4**, 56 (2002).
- [57] K. Zollner and J. Fabian, Heterostructures of graphene and topological insulators  $\text{Bi}_2\text{Se}_3$ ,  $\text{Bi}_2\text{Te}_3$ , and  $\text{Sb}_2\text{Te}_3$ , *Phys. Status Solidi B* **258**, 2000081 (2021).
- [58] Y. Li and M. Koshino, Twist-angle dependence of the proximity spin-orbit coupling in graphene on transition-metal dichalcogenides, *Phys. Rev. B* **99**, 075438 (2019).
- [59] A. David, P. Rakyta, A. Kormányos, and G. Burkard, Induced spin-orbit coupling in twisted graphene-transition metal dichalcogenide heterobilayers: Twistronics meets spintronics, *Phys. Rev. B* **100**, 085412 (2019).
- [60] P. Hohenberg and W. Kohn, Inhomogeneous electron gas, *Phys. Rev.* **136**, B864 (1964).
- [61] P. Giannozzi *et al.*, Quantum Espresso: A modular and open-source software project for quantum simulations of materials, *J. Phys.: Condens. Matter* **21**, 395502 (2009).
- [62] G. Kresse and D. Joubert, From ultrasoft pseudopotentials to the projector augmented-wave method, *Phys. Rev. B* **59**, 1758 (1999).
- [63] J. P. Perdew, K. Burke, and M. Ernzerhof, Generalized Gradient Approximation Made Simple, *Phys. Rev. Lett.* **77**, 3865 (1996).
- [64] S. Grimme, Semiempirical GGA-type density functional constructed with a long-range dispersion correction, *J. Comput. Chem.* **27**, 1787 (2006).
- [65] S. Grimme, J. Antony, S. Ehrlich, and H. Krieg, A consistent and accurate *ab initio* parametrization of density functional dispersion correction (DFT-D) for the 94 elements H-Pu, *J. Chem. Phys.* **132**, 154104 (2010).
- [66] V. Barone, M. Casarin, D. Forrer, M. Pavone, M. Sami, and A. Vittadini, Role and effective treatment of dispersive forces in materials: Polyethylene and graphite crystals as test cases, *J. Comput. Chem.* **30**, 934 (2009).